Journal of the Meteorological Society of Japan

EARLY ONLINE RELEASE

The DOI for this manuscript is
DOI:10.2151/jmsj.2024-032
J-STAGE Advance published date: July 26th, 2024
The final manuscript after publication will replace the preliminary version at the above DOI once it is available.

Multi-scale uncertainty of mesoscale convective systems in the Baiu frontal zone: A case study from June 2022

Saori NAKASHITA

Graduate School of Science, Kyoto University, Kyoto, Japan

Takeshi ENOMOTO

Disaster Prevention Research Institute, Kyoto University, Uji, Kyoto, Japan
Application Laboratory, Japan Agency for Marine-Earth Science and Technology, Yokohama, Kanagawa, Japan

Satoshi ISHII

Japan Meteorological Agency, Tokyo, Japan

July 19, 2024

Corresponding author: Saori NAKASHITA, Graduate School of Science, Kyoto University, Kitashirakawa Oiwake-cho, Sakyo-ku, Kyoto, 606-8502, Japan.
E-mail: nakashita@dpac.dpri.kyoto-u.ac.jp

Abstract

Mesoscale convective systems (MCSes) occasionally develop over the East China Sea (ECS) in the Baiu frontal zone under both the atmospheric and oceanic influence. The factors that determine their predictability have not been fully understood yet. This study investigates the uncertainties affecting two MCSes observed by research vessels on 19 June 2022 using regional ensemble simulations. These MCSes have contrasting features: the first was triggered by an atmospheric mesoscale disturbance, while the second was induced by the boundary layer destabilization over the warm Kuroshio current.

The first MCS shows high variability in the synoptic-scale uncertainties detected by the breeding ensemble. The best-performing member successfully represents the strong meso-β-scale cyclone and the frontal structure with deep moist layers. The ensemble simulations are less skillful for the second MCS than the first. The enhanced surface turbulent heat flux in the SST frontal zone is found to be significantly correlated to the precipitation due to the second MCS despite the cold bias of SST that is commonly imposed on all members. The dense upper-air information from the vessels significantly improves the representation of the sharp frontal structure associated with the first MCS, but has little impact on the second MCS probably due to the underestimation of the boundary layer moistening. This case

study indicates that the predictability of MCSes over the ECS depends on their development mechanisms, and that the incorporation of uncertainties in both the atmosphere and ocean are important for the ensemble forecasting of these MCSes.

Keywords mesoscale convective system, Baiu front, regional spectral model, ensemble data assimilation

1. Introduction

The Baiu (Meiyu) frontal zone (BFZ) has a characteristic hierarchical structure from planetary to meso- or convective scales (Ninomiya and Akiyama 1992; Ninomiya and Shibagaki 2007; Tsuji and Takayabu 2023). From a planetary-scale view, the Baiu front is located between the subtropical westerly jet and the low-level jet, and these two jets contribute to maintain a convectively unstable low pressure zone, called the monsoon trough, by the advection of warm air along the BFZ (Sampe and Xie 2010). Transient disturbances that propagate along the subtropical jet form subsynoptic-scale cloud systems, and precondition an environment favorable for the development of mesoscale convective systems (MCSes). These MCSes can lead to disasters, including floods and landslides, due to heavy rainfall; therefore, it is important to accurately predict their occurrence and development.

The studies on the predictability of MCSes during the summer monsoon based on ensemble forecasts have been mainly limited to the cases developed over the continent (Bei and Zhang 2007; Luo and Chen 2015; Zhuang et al. 2020; Ke et al. 2022, 2023). These studies agreed that the representation of

MCSes is strongly sensitive to the initial conditions even if the large-scale environment features are well represented. Ke et al. (2023) found that the initial perturbations that optimally reflected the flow-dependent nature of the BFZ were important for representing the appropriate mesoscale error growth. These initial perturbation structures affected especially the error growth of water vapor, suggesting the importance of optimal initial perturbations for forecasting of moist convections. Luo and Chen (2015) also showed that the representation of MCSes was the most sensitive to the initial moisture fields. They further demonstrated that the reproducibility of cold domes induced by the preexisting convective systems was the key feature of MCS predictability. The predictability of these continental MCSes was also found to be controlled by the orography due to regulation of the moist convections (Zhuang et al. 2020). However, because MCSes over the East China Sea (ECS) develop under the moist environment affected by both the atmosphere and ocean, the predictability of such MCSes should be different from those over land. The key factors for the predictability of oceanic MCSes remain unclear.

The moist environment over the ECS with a large amount of free tropospheric moisture is maintained by continental air from the southwest and oceanic air from the south. The southwesterly low-level jet that transports the continental air intersects the southerly winds driven by the pressure gradient force that supplies oceanic moist air, and these two airstreams form a large water vapor gradient over the ECS with respect to the dry and cold air to the north (Moteki et al. 2004a,b; Maeda et al. 2008). These moist airstreams sometimes create a moist, absolutely unstable stratification before the initiation of precipitation (Tsuji et al. 2021), and trigger the heavy rainfall in conjunction with upwelling induced by the lower inflow. This mechanism indicates that the development of individual MCSes is strongly influenced by the representation of the large-scale wind distribution and the frontal zone.

The water vapor supply from the sea surface to the boundary layer is another important factor for the development of MCSes. The ECS is characterized by a steep sea surface temperature (SST) gradient due to the warm Kuroshio current. Turbulent heat fluxes intensify over the tongue of the Kuroshio, which enhances precipitation by destabilizing the boundary layer (Sasaki et al. 2012; Kunoki et al. 2015). A warm SST also contributes to the maintenance of instability near the surface by evaporation to the inflow across the Kuroshio (Kunoki et al. 2015; Sato et al. 2016). This suggests that the distributions of wind speed and temperature near the surface have a large influence on MCSes, as does the remote moisture supply in the free troposphere.

Although the development mechanisms of MCSes over the ECS have been widely investigated, it is still difficult to accurately predict the locations and intensities of individual MCSes due to high uncertainties in moist convections and lack of the observations of vertical profiles. Kato et al. (2003) found that underestimation of moisture amount in the lower troposphere caused the poor representation of meso-β-scale convective systems in their numerical simulations. Kato and Aranami (2005) also emphasized the importance of lower moisture fields to the reproducibility of heavy rainfall in the BFZ and suggested that the sufficient vertical information would reduce the forecast failure. Their results motivate us to quantify the forecast uncertainty of MCSes using ensemble methods to compensate for the difficulty in deterministic forecasting and thereby contribute to prevention and mitigation of disaster due to heavy rainfall associated with the MCSes.

In order to identify the factors affecting the predictability of oceanic MCSes, this study investigates the role of multi-scale uncertainties in the prediction of the initiation and development of MCSes through a case study for the MCSes developed during an intensive observation campaign deploying three research vessels on 19 June 2022. Recently, Manda et al. (2024) examined the detailed environmental conditions related to the MCS observed earlier in the intensive observations, and found that the near-saturation conditions in the free troposphere played an important role in supporting the MCS development. In this study, we examine the variability in the prediction of this MCS and another one observed later through ensemble simulations for this observation period. These simulations are conducted using a limited-area atmospheric model developed at the National Center for Environmental Prediction (NCEP) with flow-dependent initial perturbations to estimate the influence of initial uncertainties from the synoptic-scale to the mesoscale. We also perform sensitivity experiments to the assimilation of the vessel observations to investigate the impact of the dense upper information on the development of the MCSes.

The remainder of this paper is organized as follows. Section 2 describes the experimental design and analysis methods. Section 3 overviews the observation campaign and the environmental features related to the MCSes on 19 June 2022. Section 4 examines the sensitivity of MCSes to the initial uncertainty through the ensemble simulations. The impact of the vessel observations on the MCS representation is investigated by the assimilation experiments as shown in Section 5. Finally, Section 6 provides a summary and discussion.

2. Methodology

2.1 Forecast model

We use the NCEP regional spectral model (RSM, Juang and Kanamitsu 1994; Juang 2000) as the forecast model. The RSM retains large-scale structures represented by a base atmospheric field from a global or coarser regional model (host model) using the perturbation method (Juang and Kanamitsu 1994; Juang et al. 1997) and orographic blending at the lateral boundaries (Hong and Juang 1998). The perturbation method calculates the time evolution of the perturbations from the base field. Juang and Hong (2001) showed that the prediction skill with the perturbation method did not depend on the domain size or the discrepancy in resolution from the host model, unlike other conventional lateral boundary treatments. This method represented reasonable monsoon rainfall over East Asia (Hong et al. 1999) and the Indochina Peninsula (Nguyen et al. 2019), indicating an advantage in simulating hierarchical phenomena such as MCSes in the BFZ. The RSM was operationally used in Hawaii and Alaska for daily weather forecasts.

The RSM achieves a high effective resolution using a double Fourier series for horizontal discretization, and it offers hydrostatic (RSM) and non-hydrostatic (MSM) options for the dynamical core (Juang 2000). The RSM governing equations are primitive equations in sigma coordinates, whereas those of the MSM are fully compressible equations with internally evolving hydrostatic sigma coordinates. Both the RSM and MSM use the same model physics, with some modifications used for the MSM (Juang et al. 1997). The physics schemes and other numerical methods are shown in Table 1.

Table 1

Fig. 1

We use the RSM for the outermost domain (D1) with a horizontal resolution of 27 km, and the MSM for inner domains D2 and D3 with resolutions of 9 and 3 km, respectively (Fig. 1a). All domains have 42 vertical layers with a model top of $\sigma \sim 0.005$. The base fields of D1 are the three-hourly forecast data by the NCEP global forecast system (GFS) initialized at every six hours in a $0.25° \times 0.25°$ horizontal resolution and 33 vertical layers. Boundary conditions, including SST and land surface variables, are also obtained from the GFS.

2.2 Ensemble perturbations

We perform ensemble simulations from 1200 UTC 18 June to investigate the influence of initial uncertainties on the MCSes that passed through the observed area. The breeding of growing modes (BGM, Toth and Kalnay 1993, 1997) is used to generate the initial ensemble perturbations. The BGM method has been adopted for operational global ensemble forecast systems at the NCEP (Toth and Kalnay 1993, 1997) and the Japan Meteorological Agency (JMA, Kyouda 2002), and can extract the directions with the largest growing ratios, called bred vectors, from the difference between unperturbed and perturbed forecasts. Bred vectors are nonlinear extensions of local Lyapunov vectors (Trevisan and Legnani 1995), and they represent structures with large error saturation levels, such as baroclinic instability, rather than structures with fast error growth, such as cumulus convection. Therefore, an ensemble with the BGM perturbations could be expected to include the true state and appropriately represent the forecast error covariance for the features comparable to or larger than synoptic scales. However, because large-scale error growth tends to dominate that of small-scale and significantly affects the meso- to convective-scale forecast uncertainty (Bei and Zhang 2007; Ke et al. 2022), the BGM perturbations are also considered to be suitable for representing initial uncertainties related to mesoscale phenomena like MCSes. For example, Saito et al. (2011) demonstrated that the BGM method for the JMA nonhydrostatic regional model offered a better prediction of intense rainfall than did the downscaling method of global ensemble forecasts.

The six-hourly breeding cycles in D1 proceed as follows. The difference between unperturbed and perturbed runs for all atmospheric prognostic variables is normalized every six hours. The magnitude of the bred vectors is evaluated using the dry total energy (TE) norm (Ehrendorfer et al. 1999)

$$\|\mathbf{x}\| = \frac{1}{2D} \int_{\sigma_\mathrm{b}}^{\sigma_\mathrm{t}} \int_D \left[u'^2 + v'^2 + \frac{c_\mathrm{p}}{T_\mathrm{r}} T'^2 + R_\mathrm{d} T_\mathrm{r} \left(\frac{p'_\mathrm{s}}{p_\mathrm{r}} \right)^2 \right] \mathrm{d}D\mathrm{d}\sigma \qquad (1)$$

where u', v', T', p'_s are the zonal wind, meridional wind, temperature, and surface pressure perturbations, respectively. The constants c_p and R_d are the specific heat at constant pressure and the gas constant for dry air. D is the verification region and indicates D2 in this study. We evaluate the TE norm between $\sigma_\mathrm{t} \sim 0.5$ and $\sigma_\mathrm{b} = 1$ using the reference temperature $T_\mathrm{r} = 300\,\mathrm{K}$ and pressure $p_\mathrm{r} = 800\,\mathrm{hPa}$ (Saito et al. 2011).

The normalization coefficients are determined by the ratios of the TE norms of the perturbations to the standard norm (=$3.0\,\mathrm{J\,kg^{-1}\,m^{-2}}$), which is approximately 10% of the climatological variance. Supersaturation, negative specific humidity, and negative cloud water mixing ratio are removed from each perturbed member at the initialization of each cycle. We generate 40 members using orthogonalization. The initial seeds of the ensemble perturbations are the differences between two states that are arbitrarily chosen from the GFS initial states from May 21 to June 30 in 2020 and 2021. The breeding cycles are repeated seven times from 0000 UTC 17 June to 1200 UTC 18 June.

Lateral boundary perturbations are known to be important for the regional ensemble forecasts to retain the magnitude of the ensemble spread near the lateral boundaries (Saito et al. 2012). Although we do not use the lateral boundary perturbations, we set the outermost domain to be much larger than the inner domains to prevent an underestimation of the inner ensemble spread. The SST or land surface are not perturbed either: all the ensemble members and the unperturbed run use the same SST and land surface conditions obtained from the GFS initial analysis at 1200 UTC 18 June.

2.3 Data assimilation

In the assimilation experiments, we use the same MSM as in the ensemble simulations but with smaller inner domains (D2b and D3b in Fig. 1b) to focus on the impact of the dense observations. We use the same six-hourly breeding ensemble for D1 as was introduced in Section 2.2, and do not conduct the assimilation in D1 because no significant improvement could be expected from using a similar resolution (27 km vs 0.25°) with fewer observations in our experiments.

We use the maximum likelihood ensemble filter (MLEF, Zupanski 2005), and we perform observation space localization using local gradients of the global cost function (Yokota et al. 2016). MLEF is an ensemble variational method that analyzes the unperturbed control run. We employ the Newton method to optimize the cost function because it has better convergence properties than does the conjugate gradient method (Enomoto and Nakashita 2024). The ensemble size is 40 plus one unperturbed member. The localization cut-off scale is 100 (D2b) or 50 (D3b) km in the horizontal direction and 0.4 $\ln p$ in the vertical direction for both domains. The analyzed ensemble perturbations are relaxed to the prior perturbations by 80% as covariance inflation (Zhang et al. 2004).

The assimilated observation sets are extracted from the NCEP PREPBUFR: reports from surface stations (surface pressure), ships and buoys (surface pressure, zonal and meridional winds), and upper-air soundings (zonal and meridional winds, temperature and specific humidity) including those from the intensive observation campaign. Because all the observation types are set to be the same as the prognostic variables, the observation operators are linear, and we limit the maximum number of iterations in the optimization to one. Fig. 2

The control experiment (CNTL) that uses all the observations described above is compared against the data denial experiment that assimilates all but the vessel observations (NOSHIP). The assimilation in D2b is initialized at 0000 UTC on the 18th by interpolation from D1, and the assimilation in D3b is at 2100 UTC on the 18th by interpolation from D2b, and both assimilations end at 0300 UTC on the 20th (Fig. 2). The cycle interval is three hours until the start of the intensive observations at 0000 UTC on the

19th, and after that, the assimilation cycle forks into CNTL and NOSHIP with shortening the cycle interval to an hour.

Our assimilation system does not analyze the SST and land surface conditions. All the ensemble members in the assimilation experiments are initialized with the SST and the land surface conditions obtained from the GFS analysis at 0000 UTC on the 19th. Hence, the differences between CNTL and NOSHIP arise from the influence of the vessel observations on the atmospheric field.

2.4 Data and analysis methods

The hourly-accumulated JMA nationwide radar composite rainfall (JMA Observations Department 2004) and the three-hourly data of the JMA operational mesoscale analysis (JMA-MA, JMA 2019) are used as a reference for the precipitation and atmospheric fields. The convective activity is evaluated using the brightness temperature (BT) as measured by the Advanced Himawari Imager (AHI) on the JMA Himawari-8 geostationary satellite. The simulated radiances from the MSM fields are generated using the radiance simulator with the RTTOV fast radiative transfer model version 13 (Saunders et al. 2018).

The representation of MCSes in each simulation is evaluated against the radar rainfall using two metrics related to the precipitation: the averaged precipitation in the observed region (128.0°–129.3°E, 30.1°–31.1°N), and the fractions skill score (FSS, Roberts and Lean 2008) applied to a 95 percentile of 6-h precipitation threshold with a neighborhood size of around 51 km in the verification region including southern Kyushu (128.0°–131.5°E, 29.5°–32.5°N). While the former measures the accuracy in both amount and location of precipitation, the latter does the correspondence of precipitation distribution with that of the JMA radar composite.

The development mechanisms of MCSes are analyzed from two perspectives: the formation of deep unstable layers due to moistening in the free troposphere and boundary layer destabilization due to the surface heat flux from the ocean. The former is measured by the existence of moist absolutely unstable layers (MAUL, Bryan and Fritsch 2000), which are defined as

$$\frac{\partial \theta_\mathrm{e}}{\partial z} < 0 \ \ \& \ \ \mathrm{RH} > 95\% \tag{2}$$

where θ_e is the equivalent potential temperature, z is the geometric height and RH is the relative humidity. MAUL is a characteristic feature of MCSes that develop in a relatively humid environment. The RH threshold in Eq. (2) is relaxed relative to that in the definition of Tsuji et al. (2021) so that the MAUL is visually consistent with the JMA-MA considering the bias in the RSM. The saturation can be alternatively evaluated by cloud or rain water (Bryan and Fritsch 2000) for the RSM, but the location of MAUL does not change significantly.

The net surface heat flux F_{es} (the sum of the sensible and latent heat flux) is estimated from the wind speed in the boundary layer ($|\mathbf{u}_{\mathrm{b}}|$) and the difference between the saturated θ_{e} at the sea surface (θ_{ess}) and θ_{e} in the boundary layer (θ_{eb}) as

$$F_{\mathrm{es}} = C_{\mathrm{d}} U_{\mathrm{e}} (\theta_{\mathrm{ess}} - \theta_{\mathrm{eb}}) = C_{\mathrm{d}} U_{\mathrm{e}} \Delta\theta_{e} \tag{3}$$

where $C_{\mathrm{d}} \sim 10^{-3}$ is the drag coefficient, $U_{\mathrm{e}} = (|\mathbf{u}_{\mathrm{b}}|^2 + W^2)^{1/2}$ is the effective wind speed, i.e., the wind speed corrected for gustiness ($W = 3\,\mathrm{m\,s^{-1}}$ in this study) in the domain (Raymond 1995). Equation (3) indicates that the sea surface flux is approximately proportional to the product of $|\mathbf{u}_{\mathrm{b}}|$ and $\Delta\theta_{\mathrm{e}}$. In the evaluation of Eq. (3), θ_{ess} is calculated using the observed or prescribed SST, and θ_{eb} and $|\mathbf{u}_{\mathrm{b}}|$ are calculated from the values on the deck for the observations, and from those at 2 m altitude above the surface for the simulations, respectively, assuming well mixed boundary layers.

3. Observed mesoscale convective systems

From June to July 2022, a field campaign was conducted in the ECS by the JMA and universities and research institutes in Japan. This campaign was part of a coordinated effort to elucidate the formation mechanism of quasi-stationary line-shaped rain bands (*Senjo-Kousuitai*, Kato 2020) in the BFZ. During this campaign, three research vessels, *Nagasaki-maru* of Nagasaki University, *Kagoshima-maru* of Kagoshima University, and *Seisui-maru* of Mie University, conducted intensive synchronized atmospheric and oceanographic observations. Their observations were designed to investigate the air-sea interaction between the BFZ and the warm Kuroshio current in the planned study called "Two-way interactions between East Asian marginal seas and atmosphere and monsoon modulations" as a part of the project "Mid-latitude ocean-atmosphere interaction hotspots under the changing climate". During this concentrated observation period, two MCSes passed through the observation area. These MCSes each had general characteristics of convective systems frequently observed in the BFZ on the ECS. The environmental features related to these MCSes are described below.

3.1 Case overview

Fig. 3

The Baiu front was located just above the observed area (at approximately 30°N) on June 19. The upper subtropical westerly jet over the Tibetan Plateau divided into two branches; the northern branch meandered largely until it reached 50°N, while the southern branch ran just south of the Baiu front over the ECS (Fig. 3a). The southwesterly lower jet (Fig. 3b) passed parallel to the southern branch in the upper troposphere (Fig. 3a) and advected a large amount of moisture from the Philippine Sea. This southern jet tilted slightly northward with height (Fig. 3c), likely due to the diabatic heating over the Baiu-frontal rainband (Sampe and Xie 2010). There were no obvious disturbances in the upper troposphere over the ECS during the campaign period. Fig. 4

Figure 4 shows the environmental features during the first (0300 UTC) and second (2100 UTC) halves of the intensive observation period. Convection was active along the front (Fig. 4a) at 0300 UTC. Two warm and moist airstreams (Fig. 4b, around 125°–129°E, 29°–30°N) that were due to southwesterlies in the lower troposphere and south-southwesterlies near the surface supplied a large amount of precipitable water, which made the environmental conditions favorable for the first MCS development (Manda et al. 2024), and generated distinct meridional water vapor gradients near 31°N over the ECS. In the lower troposphere, a trough whose axis ran along the Baiu front extended eastward from the Yangtze River estuary. A meso-β-scale cyclone (hereafter meso-β cyclone) formed at the tip of the monsoon trough and accompanied the first MCS that passed through the observed area (Fig. 4a, c).

Although the Baiu front remained at almost the same latitude, convection was less active in the middle of the ECS during the latter half of the campaign period than the first half (Fig. 4d). This suppression was due to the reduction of moisture supply by southwesterlies (Fig. 4e), and the free troposphere was relatively drier. The precipitable water was marked by two maxima: near the Yangtze estuary (121°E, 30°N) and to the south of the Kyushu region (130°E, 30°N). The moist air from the Philippine Sea was transported to the south of Kyushu by a south-southwesterly flow along the margin of the subtropical high and was further supplied moisture during the passage over the warm SST tongue of the Kuroshio. Some convective systems successively occurred near this water vapor maxima and moved along the west-southwesterlies enhanced by the cyclonic circulation centered near 33°N, 127°E (Fig. 4d, f). These convective systems merged to develop an MCS.

3.2 Observed features by the vessels

Fig. 5

The observed features by the vessels associated with the MCSes are examined. The tracks of three vessels formed a lattice network (Fig. 5). All vessels started from their southeast corners at 0000 UTC 19 June and observed at almost the same latitude simultaneously at hourly intervals. The observations continued until 0200 UTC 20 June and a total of 70 radiosondes were launched from the vessels. Kagoshima-maru (center) and

Seisui-maru (right) observed high SST (> 26.5 °C) over the tongue of the Kuroshio from 0000 to 0500 UTC 19 June (Fig. 5). The observed SST indicates steep SST gradients between Nagasaki-maru and Kagoshima-maru (128.3°E) and around 30.4°N. The initial SST analysis obtained from NCEP GFS underestimates the warm tongue of the Kuroshio and fails to represent the steep gradients (Fig. 5). This cold bias is common to the GFS analysis from June 18 to 20. As a result, all the simulations in this study significantly underestimates the warm SST effect. The effect of the SST underestimation on the MCS development will be discussed in detail in Section 4 and 5. Fig. 6

Figure 6 shows the time series of vertical profiles of horizontal winds and θ_e. During the passage of the first MCS (0200–0500 UTC), all the three vessels observe a significantly moist and warm layer reaching up to around 700 hPa. In particular, Nagasaki-maru (Fig. 6a) and Seisui-maru (Fig. 6c) detect deep MAUL from 925 to 500 hPa at 0300 UTC. In the boundary layer, θ_e rises as the approach of the MCS, and abruptly drops after the MCS passage with the change of wind direction. Surface winds gradually return from northerly to southerly in about six hours. After 0600 UTC, the lower troposphere becomes less humid than before (Fig. 4e). At the passage of the second MCS (1800–2000 UTC), Nagasaki-maru observes a relatively deep moist layer, but θ_e is lower than when the first MCS develops. Kagoshima-maru (Fig. 6b) and Seisui-maru (Fig. 6c) observe almost saturated boundary layers with θ_{e} close to 350 K, suggesting convectively unstable stratification.

Fig. 7

Time evolutions of surface wind speed, θ_{eb}, θ_{ess} and convective available potential energy (CAPE) for parcels lifted from the deck level are shown in Fig. 7. Surface wind speed is larger than 5 $\mathrm{m\,s^{-1}}$ in the first half of the observation period. During the first MCS passage, θ_{ess} observed by Kagoshima-maru and Seisui-maru is remarkably high as shown in Fig. 5, and $\Delta\theta_{\mathrm{e}}$ becomes larger than 10 K. Although Nagasaki-maru is located over the cooler SST region than the other vessels, surface wind is stronger than the others during the first two hours because of the approaching meso-β cyclone. Therefore, all the vessels indicate favorable conditions for release of the sea surface flux. The resulting heating in the boundary layer yields the largest CAPE during the observation period in Nagasaki-maru (839.5 $\mathrm{J\,kg^{-1}}$) and Kagoshima-maru (786.6 $\mathrm{J\,kg^{-1}}$) at 0200 UTC though smaller than those typically observed for MCSes over land. After that, all the vessels observe a marked decrease in θ_{eb} and CAPE due to the convection and advection of cold dry air from the north as shown in Fig. 6. The decreasing θ_{eb} gradually recovers in almost the same time scale as the surface wind direction. At 1800 UTC when the second MCS was passing, although θ_{eb} of approximately 350 K is comparable to the values at 0200 UTC, CAPE observed by Seisui-maru is almost half of the values at 0200 UTC.

4. Sensitivity to initial uncertainties

In this section, sensitivity of the MCS representation to the initial uncertainties is examined using the ensemble simulations. The key features of the MCS predictability are identified by the comparison between the unperturbed run and the best-performing members.

4.1 Ensemble variability

Fig. 8

First, we examine the ensemble variability in D2 to investigate the flow-dependent uncertainties. The ensemble spread over the ECS shows similar distributions in D2 and D3 and becomes larger in the lower troposphere. Figure 8 shows the kinetic energy and specific humidity spreads on the 850 hPa surface in D2 from the initial time to forecast time 36 h (FT36). At 1200 UTC on the 18th, the kinetic energy spread becomes large in front of the trough extending eastward from the estuary of the Yangtze River (Fig. 8a). This large spread grows further and moves eastward with the trough until FT24 (Fig. 8b, c), which could be interpreted as the uncertainty corresponding to the development of the meso-β cyclone. After that, the large spread takes an elongated form along the BFZ without distinct maxima (Fig. 8d). The water vapor spread keeps large and shows narrow maxima along the θ_e front over the ECS (Fig. 8e–h) during the simulation period. This large spread corresponds to the variability in the location of the largest meridional gradient of specific humidity, i.e., this signal represents the uncertainty in the location of the western part of the BFZ characterized by the water vapor front (Ninomiya and Akiyama 1992; Moteki et al. 2004b). The water vapor has the largest variability at FT24, and after that the spread becomes wide in the north of the ECS (Fig. 8h). The distribution of these ensemble spreads indicates that the simulated MCSes are affected by the upstream synoptic uncertainty. Fig. 9

Next, the 1-h precipitation averaged in the vessel observation area is verified against the JMA radar composite (Fig. 9). The precipitation peaks associated with the two MCSes appear at 0400 and 1900 UTC in the JMA radar composite (black bars in Fig. 9a). The unperturbed downscaling simulation (blue curve in Fig. 9a) generally follows the time evolution of the radar composite but underestimates the precipitation amounts. The 6-h precipitation amounts for the two peaks (38.1 mm and 14.9 mm) are smaller than the observation (63.0 mm and 27.1 mm) by 30% and 45%, respectively. The small FSSs of the unperturbed run (0.12 for the first and 0.0 for the second) indicate the poor representation in precipitation patterns.

For the first precipitation peak, the 40-member ensemble simulations show significant variation of predicted precipitation in both peak timings and amounts (Fig. 9a, b). Approximately one-third members (13/40) predict precipitation that is closer to the radar composite than does the unperturbed run (Fig. 9b). In addition, more than half members represent the precipitation pattern better than the unperturbed run as indicated by the higher FSSs. The 6-h precipitation amounts in the observation area and FSS are strongly correlated because the location of the precipitation peak corresponds well to the observation area (as will be shown in Fig. 10a).

For the second precipitation peak, there is small variation among members in the precipitation amounts, and most members underestimate the precipitation maxima in the observation area (Fig. 9a). All members including the unperturbed run show FSSs lower than 0.5 (Fig. 9c), indicating lower predictability of the second MCS than the first. This small variation may be partly because of the small spread in both kinetic energy and water vapor around the region where the second MCS develops (Fig. 8d, h).

4.2 Key features for the first MCS

Fig. 10

Fig. 11

The first MCS had a heavy rainfall area over 100 mm/3 h near the center of the meso-β cyclone having a minimum sea level pressure of 1006.1 hPa (Fig. 10a). Figure 11a and 11d show the latitude–height cross sections of the thermodynamic stability and winds, respectively, through the center of the cyclone at 0300 UTC of the JMA-MA. The BFZ is identified by a meridional θ_e gradient at approximately 30°N. A deep MAUL rooted in the boundary layer reaches up to 700 hPa near the BFZ (Fig. 11a) as observed by the vessels (Fig. 6). This deep MAUL developed due to the abundant water vapor supply in the middle troposphere from the southwest ocean (Fig. 4b) and the warm moist air in the lower troposphere that was advected by southerly winds toward the BFZ and then ascended along the frontal surface (Fig. 11a, d). The horizontal winds converge near 30°N with the southerly winds in the south and the easterly winds in the north, and the vertical shear of the horizontal winds is weaker below 850 hPa than above in the range of 29°–31°N due to vertical mixing by the disturbance (Fig. 11d). Consequently, the enhanced convection in the BFZ intensifies the meso-β cyclone.

In the unperturbed run, although the migration speed of the meso-β cyclone corresponds well with the JMA-MA, as does the precipitation peak, the predicted cyclone is weaker by approximately 2 hPa (with a minimum sea level pressure of 1007.9 hPa) and biased northward (Fig. 10b). This northward bias is caused by the northward migration of the predicted BFZ, with both the MAUL and wind convergence located at approximately 31°N (Fig. 11b, e). Furthermore, the meridional θ_e gradient within the boundary layer in the north of the BFZ is weaker than that of the JMA-MA, and the MAUL does not reach the surface (Fig. 11b), which indicates less active convection to intensify the meso-β cyclone. The vertical shear of zonal winds around the MAUL is consistently stronger than that of the JMA-MA owing to less vertical mixing (Fig. 11e). The inflow of high θ_e air into the BFZ in the boundary layer is also weak due to the low θ_e in the boundary layer and weak southerly winds in the south of the BFZ, which may be a factor of the boundary layer being more stable than that in the JMA-MA.

Member 40, which predicts the realistic amounts and temporal variation of precipitation (yellow-green curve in Fig. 9a) with the highest FSS of 0.69, significantly mitigates the northward bias of the meso-β cyclone; its position corresponds well with the JMA-MA, although its intensity is overestimated by 1 hPa (with a minimum sea level pressure of 1004.9 hPa, Fig. 10c). In the meridional cross section through the cyclone center, the horizontal θ_e gradient over the BFZ is much stronger than either the JMA-MA or the unperturbed run up to the middle troposphere, and a deep MAUL develops to the south of this strong gradient (Fig. 11c). There is a large horizontal shear of zonal winds and a strong convergence below the MAUL (Fig. 11f). The horizontal winds have a horizontal shear of up to 500 hPa and a weak vertical shear around the disturbance due to the strong mixing by the overly intensified meso-β cyclone. The θ_e to the south of the BFZ ($< 30°$N) in the boundary layer is still lower than that of the JMA-MA, and the MAUL does not reach the surface, nor does the unperturbed run. However, the near-surface southerly winds are stronger than those in the unperturbed run and they supply warm and moist air to the BFZ, which contributes to the formation of the MAUL in the south of the BFZ (29°–30°N, Fig. 11c,f).

4.3 Key features for the second MCS

The second MCS produced line-shaped precipitation bands elongated east-northeastward although the rainfall was moderate than that with the first MCS (Fig. 10d). Unlike the first MCS, no distinct mesoscale disturbance was present at that time. The unperturbed run generates a false meso-β cyclone to the north of the observation area (Fig. 10e). This false cyclone induces a precipitation band which is too strong over the Kyushu region. In the south of the observation area, wide-spread precipitation occurs due to overestimated precipitable water in this region (not shown). Member 10 predicts the precipitation due to the second MCS better than the other members (Fig. 9c), though the peak timing is later than observed (dark blue curve in Fig. 9a). This member represents well the surface south-southwesterlies and a line-shaped rain band along the surface wind direction (Fig. 10f). Fig. 12

The facts that the direction of surface winds and the rainband corresponds well and that the rising of θ_{e} is observed only in the boundary layer (Fig. 6) suggest that the destabilization of the boundary layer over the warm ocean is likely to play a dominant role in the convective initiation. Figure 12 compares the distribution of surface heat flux (Eq. 3) between the unperturbed run and member 10 at 2100 UTC. The unperturbed run (Fig. 12a) shows two precipitation regions, one is in the north of the observation area due to the false cyclone (Fig. 10e) and the other is in the SST frontal zone. The latter is accompanied by the local maximum of F_{es}. The large release of surface heat flux in the SST frontal zone is more evident in member 10 (Fig. 12b). This large release of the surface heat flux is due to the local maximum of both $\Delta\theta_{\mathrm{e}}$ and surface wind speed induced by large pressure gradients in the SST frontal zone (Sasaki et al. 2012). The precipitation region in member 10 is located downstream of this local maximum of the surface heat flux. There is a positive correlation (0.56) with a significance level of 0.01 between the FSS of the second MCS precipitation (Fig. 9c) and F_{es} averaged in the SST frontal zone (127°–128°E, 28.8°–29.8°N) during the same period. This relationship suggests that the surface heat flux in the SST frontal zone is an important factor for the predictability of the second MCS. However, the simulated flux has some limitations because both simulations fail to reproduce a large flux ($> 500\ \mathrm{K\,m\,h^{-1}}$) observed by Seisui-maru (dots at 129.3°E, 31°N in Fig. 12) due to the underestimation of SST (Fig. 5). To clarify the influence of the ocean uncertainty on the second MCS, sensitivity experiments to SST are required, which is out of scope of this study.

5. Impact of intensive observations

This section investigates the effect of dense upper observations by the three vessels on the representation of the MCSes through the assimilation experiments.

5.1 Overall DA impact

Fig. 13

Impacts of the upper observations are displayed by variables in the time–height cross section of the horizontally averaged ensemble spread difference (CNTL − NOSHIP) in D2b (Fig. 13). Blue layers indicate a decrease in spread, i.e., uncertainty reduction that is attributable to the assimilation of the intensive observations. The CNTL spreads in zonal winds (Fig. 13a) and temperature (Fig. 13c) in the bottom layers begin to decrease compared with NOSHIP from 0400 UTC on the 19th, which may correspond to the abrupt change in temperature and wind direction with the meso-β cyclone passage (Fig. 6). The difference between the two experiments becomes larger for all variables after 1200 UTC. For the wind components (Fig. 13a, b), a uniform spread reduction below 850 hPa is observed after 1500 UTC, whereas the reduction in the temperature spread (Fig. 13c) is relatively small but significant in the bottom layers. The spread of specific humidity (Fig. 13d) reduces more significantly and more widely than that of the other variables. Overall, it is found that the impact of the vessel observations is large in the lower troposphere and has a large impact on water vapor. Fig. 14

Figure 14a–d shows the ensemble spread of CNTL on the 850 hPa surface averaged over the assimilation period in D2b. The zonal (Fig. 14a) and meridional (Fig. 14b) wind spreads are large to the east (31°N, 125°–127°E) and to the southwest (28°–30°N, 119°–121°E) of the trough extending from the continent (approximately 30°N, Fig. 8a), where the horizontal gradient of wind speed is large. The former is more pronounced for zonal winds and the latter for meridional winds. The spread maximum to the east of the trough probably represents the uncertainty of the position of horizontal wind shear due to the migration of the trough axis, and that to the southwest of the trough represent the uncertainty of the southerly winds carrying warm and moist air across the continent. In contrast, the spreads of both temperature (Fig. 14c) and specific humidity (Fig. 14d) reach their maximum over the strong meridional θ_{e} gradient in the western ECS (Fig. 8e–h) and represent the uncertainty in the position of the front.

The spread difference between CNTL and NOSHIP (Fig. 14e–h) is concentrated around the observation area and its east (downstream) side for all variables except for specific humidity (Fig. 14h). The spread reduction in zonal winds (Fig. 14e) is larger than the other variables and extends zonally along the trough axis. The spread reduction in meridional winds (Fig. 14f), temperature (Fig. 14g), and specific humidity (Fig. 14h) commonly peaks to the southwest of the observation area, corresponding to the southwesterly advection of warm and moist air. Changes in the specific humidity spread are also significant in the frontal zone upstream of the observation area, where the spread in CNTL is smaller to the north and larger to the south of the spread maximum than that in NOSHIP (Fig. 14h). This dipole spread change indicates southward movement of the spread maximum in CNTL relative to NOSHIP, and it could be interpreted to mean that the ensemble mean position of the front is located more southward in CNTL than in NOSHIP. The fact that only the specific humidity spread changes along the front is consistent with the characteristics of the water vapor front on the western part of the BFZ. These results indicate that the range of the influence of observation differs depending on the variables. The localization radius is common to all variables in this study, but the variable-dependent localization radius could have been alternatively used (Wang and Wang 2023).

5.2 Impact on the predictability of MCSes

Fig. 15

The MCS representations in the assimilation experiments are evaluated using precipitation (Fig. 15). All members in NOSHIP including the unperturbed analysis underestimate the precipitation peak associated with the first MCS around 0400 UTC (Fig. 15a). By contrast, CNTL shows an abrupt increase in precipitation at 0400 UTC, and more than 75% of the members in CNTL predict a larger amount of precipitation than the radar composite at 0500 UTC, although the predicted precipitation peak is delayed by an hour relative to the observed peak. Although the impact of observations accumulates (Fig. 13), the second precipitation peak around 1900 UTC is not reproduced by either CNTL or NOSHIP. Note that the increase in precipitation from 2100 to 2300 UTC in NOSHIP is due to the formation of a false meso-β cyclone near the observation area (not shown) and does not represent the second peak associated with line-shaped rain bands (Fig. 10d). The difference in the impact of the vessel observations between the first and second MCSes is also clear in FSS (Fig. 15b, c). For the first MCS (Fig. 15b), the vessel observations significantly improve the representation of realistic precipitation in terms of both the amounts and patterns. For the second MCS (Fig. 15c), on the other hand, the vessel observations make little difference between the two experiments though the assimilation of conventional observations helps to produce better predictions of precipitation than the ensemble forecasts (Fig. 9c). Fig. 16

We look into the difference of the first MCS representation between CNTL and NOSHIP. Figure 16 compares the 1-h accumulated precipitation, sea level pressure, and surface winds from 0100 to 0500 UTC 19 June between the radar composite with the JMA-MA, CNTL and NOSHIP. Both

CNTL and NOSHIP predict a small-scale cyclone developing around the western edge of the observation area and heavy local rainfall at the cyclone at 0100 to 0300 UTC. However, compared with the widespread radar rainfall, both CNTL and NOSHIP underestimate the amount of precipitation averaged over the observation area (Fig. 15). In addition, the predicted cyclone at 0300 UTC in CNTL and NOSHIP is smaller than that in the JMA-MA in diameter of an outer closed isobar (approximately 30 km vs 100 km) although the cyclone location corresponds well. The difference between CNTL and NOSHIP is unclear up to this time, but NOSHIP shows a slightly faster eastward migration of the cyclone than does the JMA-MA. After the passage of the MCS through the observation area at 0300 UTC, CNTL has an obvious advantage over NOSHIP consistent with Fig. 15, and reproduces convective cells elongated in the southwest-northeast direction and strong surface wind shear associated with the developed meso-β cyclone, whereas the cyclone in NOSHIP decays after 0400 UTC. Fig. 17

The difference between CNTL and NOSHIP in the first MCS representation is clear in the distribution of convection. Figure 17 shows the observed or simulated Himawari-8 AHI channel 13 BT, which represents the cloud-top height. A convective system located upstream of the observation area at 0100 UTC develops and moves eastward while merging with the small convective system on the south side of the observation area to develop into a single zonally extended MCS (Fig. 17a). Although the MSM has an overall shallow bias in cloud-top height (high BT), deep convective clouds with BT of approximately 210 K develop at 0400 UTC in CNTL (Fig. 17b), corresponding well to the observed clouds (Fig. 17a), whereas NOSHIP fails to represent deep clouds (Fig. 17c). The improvement in CNTL against NOSHIP is concentrated on the downstream side of the vessel observations, which is consistent with the large spread reduction in Fig. 14. Fig. 18

The assimilation of the vessel observations improves not only the unperturbed analysis but also the ensemble members. Figure 18 shows the probability of deep convection. Here BT of 215 K (white contours in Fig. 18) is chosen as a proxy for deep convection, and the ratio of the number of members that predict BT $<$ 215 K to the ensemble size is shown in color shades. Few members of either CNTL or NOSHIP represent the upstream convective system in the earlier cycles, resulting in low reproducibility of the MCS until 0300 UTC. However, approximately one-third of the CNTL members represent deep convection just over the observation area (near 129°E, 30.5°N) at 0300 UTC (Fig. 18a), whereas almost all members in NOSHIP still do not predict deep convection as observed. After that, the number of members in CNTL simulating deep convection increases rapidly with the assimilation cycles, and more than 80% predict deep convection to the east of the observation area (129°–130°E, 30.5°–31.5°N) at 0500 UTC.

This high probability within the observed deep convective area indicates an increase in the number of successful ensemble members in the representation of the MCS because of the assimilation of the vessel observations. Fig. 19

Next, we investigate the reason for the difference between the two experiments in the representation of the first MCS. Figure 19 shows the difference in the first analysis between CNTL and NOSHIP, i.e., the increment due to the vessel observations at 0000 UTC on the 19th. The wind increments in the lower troposphere (Fig. 19a) yield southerly winds to the south and easterly winds over and to the north of the observation area. These easterly winds enhance the horizontal wind shear in the frontal zone (Fig. 11d). The wind direction of the increments has a cyclonic shear and induces convergence to the west of the observation area, which is consistent with the initiation of upstream convection. The increments in temperature and specific humidity are also shown in the latitude–height (Fig. 19b) and longitude–height (Fig. 19c) cross sections. The temperature and specific humidity increments have a larger variation in the meridional rather than the zonal direction. The temperature increment takes a dipole pattern across the front (29°–30°N) with a positive increment in the south and a negative increment in the north, strengthening the frontal structure. The specific humidity increment moistens below 850 hPa in the frontal zone and supports the formation of MAUL. Thus, the vessel observations contribute to a favorable environment for developing the first MCS from the initial cycle.

Fig. 20

Fig. 21

The increments by the vessel observations yield clear differences in the environmental features between CNTL and NOSHIP at 0300 UTC on the 19th, just before the conspicuous improvement of the first MCS in CNTL. Figure 20 shows the distribution of precipitable water and the vertically integrated water vapor flux of (a) CNTL and (b) NOSHIP. CNTL represents a larger amount of precipitable water over the observation area and to its west than does NOSHIP, which is favorable for the development of the MCS. Figure 21 shows the latitude–height cross section (the same location as Fig. 11) of the (a, c) thermodynamic and (b, d) wind fields. NOSHIP has MAUL with a northward bias (Fig. 21c), as does the downscaling from 1200 UTC on the 18th (Fig. 11b) due to a less steep meridional θ_{e} gradient and a weak lower convergence (Fig. 21d). Figure 21c also shows that the boundary layer is relatively cold and dry compared with that of the JMA-MA (Fig. 11a) because of the weak southerly flow near the surface (Fig. 21d). CNTL (Fig. 21a) mitigates this northward bias of MAUL and has a steep frontal structure similar to that of the JMA-MA. This frontal structural change is consistent with the increment in Fig. 19. CNTL also has stronger near-surface southerly flow into the BFZ and convergence below the MAUL (Fig. 21b) than those in NOSHIP. These wind structures enhance the heating and moistening of the boundary layer and the upward motion of this warm moist air, supporting the formation of the deep MAUL. These results indicate that the assimilation of dense observations by the vessels significantly improves the representation of the MCS mainly by correcting the atmospheric frontal structure. Note that the vessel observations have little impact on the improvement in the upstream MCS at 0100–0300 UTC on the 19th. Although the cumulative impact of the observations is certainly important, this failure is partly due to the significant underestimation of the upstream moisture content (Fig. 20a, b) compared to the JMA-MA (Fig. 4b), which is largely determined by large-scale circulations. These large-scale features are difficult to modify only by the local observations from the vessels.

As shown in Fig. 15, the representation of the second MCS is relatively insensitive to the vessel observations. Although the assimilation of the vessel observations in CNTL helps to reproduce the realistic south-southwesterly flow near the surface and the convective initiation in the downstream region, the predicted convections decay faster than the observed (not shown). As discussed above, the second MCS can be considered to be driven by the continuous moisture supply from the warm tongue of the Kuroshio (Fig. 12). Although the vessel observations increase the moisture amounts in the south of the observation area (Fig. 20c, d), they cannot contribute to represent the significantly large amount of moisture where the second MCS has matured (around 130°E, 30°N, Fig. 4d, e). The importance of the boundary layer will be examined in the next section.

5.3 Comparison with the observations

Fig. 22

The time series of vertical profiles of the analyzed field of the two experiments (Fig. 22) are compared against radiosondes from the three vessels (Fig. 6). CNTL (Fig. 22a–c) successfully represents the deep layer with high θ_e and abrupt temperature change after the first MCS passage, although the lower wind direction changes are not sufficiently reproduced. NOSHIP (Fig. 22d–f) also shows a slight increase in θ_e at the location of Nagasaki-maru (Fig. 22d), but θ_e remains lower at the other two ships' locations and the moist layer is shallower than that of the observations. Therefore, the first MCS does not develop well and θ_e hardly decreases after the passage. At the time of the second MCS passage, CNTL fails to reproduce the rise in θ_e below 925 hPa observed by Kagoshima-maru and Seisui-maru (Fig. 6b, c), while NOSHIP maintains high θ_e at lower levels close to the observations at the time of the second MCS passage (Fig. 22d–f) due to the poor development of the first MCS, and this high θ_e probably leads to generating the false meso-β cyclone.

Fig. 23

Figure 23 shows the surface wind speed, θ_{eb}, θ_{ess}, and CAPE in the two assimilation experiments equivalent to those of the vessel observations (Fig. 7). The surface wind speed of CNTL (Fig. 23a) corresponds well to that of the observations (Fig. 7) throughout the observation period and increases with the passage of the first MCS. The wind speed also increases in accordance with Kagoshima-maru and Seisui-maru when the second MCS passes, despite the precipitation amounts being underestimated. NOSHIP (Fig. 23b) shows a flat wind speed except at the end of the observation period due to the development of the false cyclone. CNTL also reproduces the abrupt increase in CAPE just before the first MCS due to the heating in the boundary layer (Fig. 23a), which are consumed by the development of intense convections. On the other hand, CAPE increases more slowly in NOSHIP than in CNTL, and the moderate CAPE ($\sim 400\ \mathrm{J\,kg^{-1}}$) is kept until the false cyclone passage in NOSHIP (Fig. 23b).

In contrast to the wind speed and CAPE, there are clear differences between the observations and experiments in θ_{eb} and θ_{ess}. The θ_{ess} values in the experiments are always cooler than the observed values and fluctuate little in contrast to the observed variation (Fig. 7) because the SST used in the experiments is cooler and smaller in its spatial variation than that observed (Fig. 5). Furthermore, the θ_{ess} differences between the experiments are small because they only reflect the difference in sea level pressure. The θ_{eb} variations in CNTL are similar to those of the observations to some extent.

θ_{eb} increases before the passage of the first MCS and then decreases from 0500 to 0700 UTC in CNTL. $\Delta\theta_{\mathrm{e}}$ becomes positive with this drop in θ_{eb}, which makes conditions more favorable for the sea surface flux than those in NOSHIP. However, because θ_{ess} is lower and its decrease is slower than that of the observations, the time when $\Delta\theta_{\mathrm{e}}$ reaches its maximum is later than the time of the first MCS passage, and the sea surface flux is downward ($\Delta\theta_{\mathrm{e}} < 0$) at that time. Therefore, the contribution of sea surface flux to the development of the predicted MCS is limited in CNTL. Nevertheless, the presence of a deep moist layer contributes significantly to the first MCS development, as discussed above, and this creates an observable difference between CNTL and NOSHIP in the first MCS representation. In the later observation period, both θ_{ess} and θ_{eb} fluctuate little, which is unfavorable to the release of the sea surface flux in either experiment. These results suggest that the effect of the surface heat flux from the warm ocean is underestimated for both MCSes in the assimilation experiments.

6. Summary and discussion

In this study, we performed nested ensemble simulations and ensemble data assimilation experiments for the MCSes in the BFZ using the NCEP regional spectral model. Two MCSes were captured by radiosondes launched hourly by three research vessels from 0000 UTC 19 to 0200 UTC 20 June

2022 over the ECS. These MCSes have contrasting features: the first one was accompanied by a meso-β-scale cyclone, and the other consisted of some convective systems developing over the warm tongue of the Kuroshio.

This case study indicates that the predictability of the MCSes on the ECS depends on their development mechanisms. The development of the first MCS was mainly dominated by atmospheric features such as the meso-β cyclone that formed in front of the synoptic-scale trough and the formation of a deep moist unstable layer due to abundant moisture supply to the lower and middle troposphere. Hence, the synoptic-scale ensemble perturbations that reflect the uncertainties in the trough or water vapor front were able to represent the uncertainty of the MCS and showed significant variations in both the location and intensity of the MCS. A member with a more accurate representation of the MCS than the unperturbed run improved the representation of the strong meso-β cyclone and the frontal structure with steep meridional θ_e gradient and deep MAUL.

In addition, dense upper soundings by the three research vessels significantly influenced the reproducibility of the first MCS. The vessel observations had a significant impact on the lower troposphere and the downstream region. The influence of the observations on precipitation became clear just after the passage of the MCS. The unperturbed analysis of the CNTL represented a strong meso-β cyclone with realistic deep convection elongated in the southwest-northeast direction, whereas a meso-β cyclone in the NOSHIP decayed fast. The difference between CNTL and NOSHIP in the representation of the MCS was also clear among the ensemble members. More than 80% of the CNTL ensemble members showed deep simulated convective clouds that corresponded well to the satellite observations. The increments due to the vessel observations steepened the front and moistened the frontal zone to increase the amount of precipitable water. These changes contributed to the formation of deep moist unstable layers and to the development of the MCS as suggested in Manda et al. (2024). However, intensive observations alone cannot improve the upstream MCS because of the significantly underestimated upstream moisture determined by large-scale circulations. These large-scale circulations are usually represented better in a global analysis than in a regional analysis because of the global coverage of the observation network, so an appropriate treatment of the global analysis in regional assimilations could improve the upstream representation in the BFZ, which will be addressed in future work.

In contrast to the first MCS, the second MCS has low reproducibility in both ensemble simulations and assimilations. The best-performing member in the ensemble simulations represented the large amount of surface heat flux in the SST frontal zone, and the heat flux in this zone was positively correlated to the precipitation patterns associated with the second MCS.

This suggests the importance of the sharp frontal structure in SST for the development of the second MCS. However, the comparison of simulations with the observations revealed that the heat supply from the warm ocean to the boundary layer was underestimated throughout the observation period due to a cold SST bias in the warm Kuroshio current imposed on all simulations. This underestimation of the ocean influence may result in the unclear impact of the vessel observations on the second MCS. Therefore, improving the prediction of this MCS would require SST to be as accurate as possible. However, accurate SST in the BFZ is difficult to obtain because SST observations rely largely on the microwave sounders that cannot measure SST under heavy rainfall conditions. As a result, there is significant variability in the representation of SST over the ECS in the Baiu season between the different products. To represent the uncertainty of the SST, the ensemble of SST should be considered like the atmospheric ensemble. Kunii and Miyoshi (2012) and Duc et al. (2015) showed that SST perturbations had positive impacts on both the typhoon track and intensity forecasts. The SST ensemble could also be useful for evaluating the influence of the uncertainty in the SST on the MCS. Whereas the multi-center SST ensemble reflects the uncertainty of the observations, ocean dynamics also has its own growing modes. Although a fully coupled atmospheric-ocean assimilation system may be able to introduce the influence of ocean dynamical uncertainty into atmospheric variability, determining the impact of atmospheric observations on the ocean or vice versa is complicated (Komori et al. 2018). Ohishi et al. (2023) produced an ensemble analysis product called local ensemble transform Kalman filter-based ocean research analysis (LORA) to incorporate oceanographic dynamic uncertainty into the estimation of analysis uncertainty. Such ensemble products would be useful for simply reflecting the impact of ocean uncertainty on atmospheric disturbances. Furthermore, we should consider the uncertainties in the surface physics and planetary boundary layer schemes since the effect of surface heat flux on the atmosphere is determined by surface conditions and vertical diffusion. The sensitivity experiments that take into consideration the uncertainties in SST and physics schemes will be reported elsewhere.

Data availability statement

All data from the ensemble experiments by the NCEP MSM will be provided upon request. The NCEP GFS forecast data and PREPBUFR were obtained from the National Oceanic and Atmospheric Administration (NOAA) Operational Model Archive Distributed System (NOMADS). The data in June 2022 are currently available at the National Center for Atmospheric Research (NCAR) Research Data Archive (RDA). The radar composite rainfalls and the mesoscale operational analysis of the JMA were obtained from the database of Research Institute for Sustainable Humanosphere, Kyoto University. Himawari-8 gridded data was obtained from the P-tree System of the Japan Aerospace Exploration Agency. These data are available at the following URLs:

Radar: `http://database.rish.kyoto-u.ac.jp/arch/jmadata/data/jma-radar/synthetic/original/`

JMA mesoscale analysis: `http://database.rish.kyoto-u.ac.jp/arch/jmadata/data/gpv/original/`

Himawari-8: `https://www.eorc.jaxa.jp/ptree/index.html`

Acknowledgements

We would like to thank all the researchers involved in the observation campaign in June 2022. The NCEP regional spectral model was provided by Dr. Hann-Ming Henry Juang. The NCEP GFS forecast data and PREPBUFR were obtained from the National Oceanic and Atmospheric Administration (NOAA) Operational Model Archive Distributed System (NOMADS). Research products of brightness temperature produced from Himawari data were supplied by the P-Tree System, Japan Aerospace Exploration Agency (JAXA). The radar composite rainfalls and the mesoscale operational analysis data of the JMA were collected and distributed by Research Institute for Sustainable Humanosphere, Kyoto University.

This work is supported by JSPS KAKENHI Grant number 22KJ1966, 19H05698, 19H05605, and 21K03662.

References

Asselin, R., 1972: Frequency filter for time integrations. *Mon. Wea. Rev.*, **100**, 487–490.

Bei, N., and F. Zhang, 2007: Impacts of initial condition errors on mesoscale predictability of heavy precipitation along the Mei-Yu front of China. *Quart. J. Roy. Meteor. Soc.*, **133**, 83–99.

Bryan, G. H., and J. M. Fritsch, 2000: Moist absolute instability: The sixth static stability state. *Bull. Amer. Meteor. Soc.*, **81**, 1207–1230.

Chou, M.-D., and M. J. Suarez, 1999: A solar radiation parameterization for atmospheric studies. *NASA Tech. Rep. Series on Global Modeling and Data Assimilation*, **15**, NASA/TM-1999-104606.

Duc, L., T. Kuroda, K. Saito, and T. Fujita, 2015: Ensemble Kalman Filter data assimilation and storm surge experiments of tropical cyclone Nargis. *Tellus A*, **67**, doi:10.3402/tellusa.v67.25941.

Ehrendorfer, M., R. M. Errico, and K. D. Raeder, 1999: Singular-vector perturbation growth in a primitive equation model with moist physics. *J. Atmos. Sci.*, **56**, 1627–1648.

Ek, M. B., K. E. Mitchell, Y. Lin, E. Rogers, P. Grunmann, V. Koren, G. Gayno, and J. D. Tarpley, 2003: Implementation of Noah land surface model advances in the National Centers for Environmental Prediction operational mesoscale Eta model. *J. Geophys. Res.: Atmos.*, **108**, 1–16, doi:10.1029/2002JD003296.

Enomoto, T., and S. Nakashita, 2024: Application of exact newton optimisation to the maximum likelihood ensemble filter. *Tellus A*, **76**, 42–56.

Ferrier, B., Y. Jin, Y. Lin, T. Black, E. Rogers, and G. DiMego, 2002: Implementation of a new grid-scale cloud and precipitation microphysics in the NCEP Eta model. Preprints, *19th Conf. on Weather Analysis and Forecasting/15th Conf. on Numerical Weather Prediction*, 10.1.

Hong, S.-Y., and H.-M. H. Juang, 1998: Orography blending in the lateral boundary of a regional model. *Mon. Wea. Rev.*, **126**, 1714–1718.

Hong, S.-Y., H.-M. H. Juang, and D.-K. Lee, 1999: Evaluation of a regional spectral model for the east Asian monsoon case studies for July 1987 and 1988. *J. Meteor. Soc. Japan*, **77**, 553–572.

Hong, S.-Y., and H.-L. Pan, 1996: Nonlocal boundary layer vertical diffusion in a medium-range forecast model. *Mon. Wea. Rev.*, **124**, 2322–2339.

Hong, S.-Y., and H.-L. Pan, 1998: Convective trigger function for a mass-flux cumulus parameterization scheme. *Mon. Wea. Rev.*, **126**, 2599–2620.

Ikawa, M., 1988: Comparison of some schemes for nonhydrostatic models with orography. *J. Meteor. Soc. Japan*, **66**, 753–776.

Japan Meteorological Agency, 2019: Outline of the operational numerical weather prediction at the Japan Meteorological Agency. [Available at `https://www.jma.go.jp/jma/jma-eng/jma-center/nwp/outline2019-nwp/index.htm`.].

Japan Meteorological Agency Observations Department, 2004: 1 km mesh zenkoku gousei radar gpv no teikyoutou ni tsuite (data provision of nationwide composited radar grid point value with 1 km resolutions). [Available at `https://www.data.jma.go.jp/add/suishin/jyouhou/pdf/162.pdf`.].

Juang, H.-M. H., 2000: The NCEP mesoscale spectral model: A revised version of the nonhydrostatic regional spectral model. *Mon. Wea. Rev.*, **128**, 2329–2362.

Juang, H.-M. H., and S.-Y. Hong, 2001: Sensitivity of the NCEP regional spectral model to domain size and nesting strategy. *Mon. Wea. Rev.*, **129**, 2904–2922.

Juang, H.-M. H., S.-Y. Hong, and M. Kanamitsu, 1997: The NCEP regional spectral model: An update. *Bull. Amer. Meteor. Soc.*, **78**, 2125–2144.

Juang, H.-M. H., and M. Kanamitsu, 1994: The NMC nested regional spectral model. *Mon. Wea. Rev.*, **122**, 3–26.

Kato, T., 2020: Quasi-stationary band-shaped precipitation systems, named “Senjo-Kousuitai”, causing localized heavy rainfall in Japan. *J. Meteor. Soc. Japan*, **98**, 485–509.

Kato, T., and K. Aranami, 2005: Formation factors of 2004 Niigata-Fukushima and Fukui heavy rainfalls and problems in the predictions using a cloud-resolving model. *SOLA*, **1**, 1–4.

Kato, T., M. Yoshizaki, K. Bessho, T. Inoue, Y. Sato, and X-BAIU-01 observation group, 2003: Reason for the failure of the simulation of heavy rainfall during X-BAIU-01 —Importance of a vertical profile of water vapor for numerical simulations—. *J. Meteor. Soc. Japan*, **81**, 993–1013.

Ke, J., M. Mu, and X. Fang, 2022: Impact of optimally growing initial errors on the mesoscale predictability of heavy precipitation events along the Mei-Yu front in China. *Mon. Wea. Rev.*, **150**, 2399–2421.

Ke, J., M. Mu, and X. Fang, 2023: Influence of physically constrained initial perturbations on the predictability of Mei-Yu heavy precipitation. *Mon. Wea. Rev.*, **151**, 2115–2138.

Kim, Y.-J., and A. Arakawa, 1995: Improvement of orographic gravity wave parameterization using a mesoscale gravity wave model. *J. Atmos. Sci.*, **52**, 1875–1902.

Komori, N., T. Enomoto, T. Miyoshi, A. Yamazaki, A. Kuwano-Yoshida, and B. Taguchi, 2018: Ensemble-based atmospheric reanalysis using a global coupled atmosphere-ocean GCM. *Mon. Wea. Rev.*, **146**, 3311–3323.

Kunii, M., and T. Miyoshi, 2012: Including uncertainties of sea surface temperature in an ensemble Kalman filter: A case study of Typhoon Sinlaku (2008). *Wea. Forecasting*, **27**, 1586–1597.

Kunoki, S., A. Manda, Y.-M. Kodama, S. Iizuka, K. Sato, I. Fathrio, T. Mitsui, H. Seko, Q. Moteki, S. Minobe, and Y. Tachibana, 2015: Oceanic influence on the Baiu frontal zone in the East China Sea. *J. Geophys. Res.: Atmos.*, **120**, 449–463.

Kyouda, M., 2002: The ensemble prediction system for medium-range weather forecasting at JMA. *Research Activities in Atmospheric and Oceanic Modelling*. Ritchie, H. (ed.), Report No.32, WMO/TD-No. 1105.

Luo, Y. and Y. Chen, 2015: Investigation of the predictability and physical mechanisms of an extreme-rainfall-producing mesoscale convective system along the Meiyu front in East China: An ensemble approach. *J. Geophys. Res.: Atmos.*, **120**, 10,593–10,618.

Maeda, S., K. Tsuboki, Q. Moteki, T. Shinoda, H. Minda, and H. Uyeda, 2008: Detailed structure of wind and moisture fields around the Baiu frontal zone over the East China Sea. *SOLA*, **4**, 141–144.

Manda, A., Y. Tachibana, H. Nakamura, T. Takikawa, A. Nishina, Q. Moteki, N. Zhao, and S. Iizuka, 2024: Intensive radiosonde observations of environmental conditions on the development of a mesoscale convective system in the Baiu frontal zone. *Earth Space Sci.*, **11**, e2023EA003486, doi:10.1029/2023EA003486.

Mlawer, E. J., S. J. Taubman, P. D. Brown, M. J. Iacono, and S. A. Clough, 1997: Radiative transfer for inhomogeneous atmospheres: RRTM, a validated correlated-k model for the longwave. *J. Geophys. Res.: Atmos.*, **102**, 16663–16682.

Moteki, Q., H. Uyeda, T. Maesaka, T. Shinoda, M. Yoshizaki, and T. Kato, 2004a: Structure and development of two merged rainbands observed over the East China Sea during X-BAIU-99 Part I: Meso-β-scale structure and development processes. *J. Meteor. Soc. Japan*, **82**, 19–44.

Moteki, Q., H. Uyeda, T. Maesaka, T. Shinoda, M. Yoshizaki, and T. Kato, 2004b: Structure and development of two merged rainbands observed over the East China Sea during X-BAIU-99 Part II: Meso-α-scale structure and build-up processes of convergence in the Baiu frontal region. *J. Meteor. Soc. Japan*, **82**, 45–65.

Nguyen, T. V., K. V. Mai, P. N. B. Nguyen, H.-M. H. Juang, and D. V. Nguyen, 2019: Evaluation of summer monsoon climate predictions over the Indochina Peninsula using regional spectral model. *Wea. Climate Extremes*, **23**, doi:10.1016/j.wace.2019.100195.

Ninomiya, K., and T. Akiyama, 1992: Multi-scale features of Baiu, the summer monsoon over Japan and the east Asia. *J. Meteor. Soc. Japan*, **70**, 467–495.

Ninomiya, K., and Y. Shibagaki, 2007: Multi-scale features of the Meiyu-Baiu front and associated precipitation systems. *J. Meteor. Soc. Japan*, **85B**, 103–122.

Ohishi, S., T. Miyoshi, and M. Kachi, 2023: LORA: A local ensemble transform Kalman filter-based ocean research analysis. *Ocean Dyn.*, **73**, 117–143.

Pan, H.-L., and W.-S. Wu, 1995: Implementing a mass flux convective parameterization package for the NMC medium-range forecast model. *NMC office note*, **No. 409**, 40 pp.

Raymond, D. J., 1995: Regulation of moist convection over the west Pacific warm pool. *J. Atmos. Sci.*, **52**, 3945–3959.

Robert, A., J. Henderson, and C. Turnbull, 1972: An implicit time integration scheme for baroclinic models of the atmosphere. *Mon. Wea. Rev.*, **100**, 329–335.

Roberts, N. M., and H. W. Lean, 2008: Scale-selective verification of rainfall accumulations from high-resolution forecasts of convective events. *Mon. Wea. Rev.*, **136**, 78–97.

Saito, K., M. Hara, M. Kunii, H. Seko, and M. Yamaguchi, 2011: Comparison of initial perturbation methods for the mesoscale ensemble prediction system of the Meteorological Research Institute for the WWRP Beijing 2008 Olympics Research and Development Project (B08RDP). *Tellus A*, **63**, 445–467.

Saito, K., H. Seko, M. Kunii, and T. Miyoshi, 2012: Effect of lateral boundary perturbations on the breeding method and the local ensemble transform Kalman filter for mesoscale ensemble prediction. *Tellus A*, **64**, doi:10.3402/tellusa.v64i0.11594.

Sampe, T., and S.-P. Xie, 2010: Large-scale dynamics of the Meiyu-Baiu rainband: Environmental forcing by the westerly jet. *J. Climate*, **23**, 113–134.

Sasaki, Y. N., S. Minobe, T. Asai, and M. Inatsu, 2012: Influence of the Kuroshio in the East China Sea on the early summer (Baiu) rain. *J. Climate*, **25**, 6627–6645.

Sato, K., A. Manda, Q. Moteki, K. K. Komatsu, K. Ogata, H. Nishikawa, M. Oshika, Y. Otomi, S. Kunoki, H. Kanehara, T. Aoshima, K. Shimizu, J. Uchida, M. Shimoda, M. Yagi, S. Minobe, and Y. Tachibana, 2016: Influence of the Kuroshio on mesoscale convective systems in the Baiu frontal zone over the East China Sea. *Mon. Wea. Rev.*, **144**, 1017–1033.

Saunders, R., J. Hocking, E. Turner, P. Rayer, D. Rundle, P. Brunel, J. Vidot, P. Roquet, M. Matricardi, A. Geer, N. Bormann, and C. Lupu, 2018: An update on the RTTOV fast radiative transfer model (currently at version 12). *Geosci. Model Dev.*, **11**, 2717–2737.

Tatsumi, Y., 1986: A spectral limited area model with time-dependent lateral boundary conditions. *J. Meteor. Soc. Japan*, **64A**, 473–483.

Tiedtke, M., 1983: The sensitivity of the time-mean large-scale flow to cumulus convection in the ECMWF model. *Workshop on Convection in Large-scale Numerical Models, 28 November to 1 December 1983* 297–316.

Toth, Z., and E. Kalnay, 1993: Ensemble forecasting at NMC: The generation of perturbations. *Bull. Amer. Meteor. Soc.*, **74**, 2317–2330.

Toth, Z., and E. Kalnay, 1997: Ensemble forecasting at NCEP and the breeding method. *Mon. Wea. Rev.*, **125**, 3297–3319.

Trevisan, A., and R. Legnani, 1995: Transient error growth and local predictability: A study in the Lorenz system. *Tellus A*, **47**, 103–117.

Tsuji, H., and Y. N. Takayabu, 2023: A hierarchical structure of the heavy rainfall event over Kyushu in July 2020. *J. Meteor. Soc. Japan*, **101**, 271–287.

Tsuji, H., Y. N. Takayabu, R. Shibuya, H. Kamahori, and C. Yokoyama, 2021: The role of free-tropospheric moisture convergence for summertime heavy rainfall in western Japan. *Geophys. Res. Lett.*, **48**, e2021GL095030, doi:10.1029/2021GL095030.

Wang, Y., and X. Wang, 2023: Simultaneous multiscale data assimilation using scale- and variable-dependent localization in EnVar for convection allowing analyses and forecasts: Methodology and experiments for a tornadic supercell. *J. Adv. Model. Earth Syst.*, **15**, e2022MS003430, doi:10.1029/2022MS003430.

Yokota, S., M. Kunii, K. Aonashi, and S. Origuchi, 2016: Comparison between four-dimensional LETKF and ensemble-based variational data assimilation with observation localization. *SOLA*, **12**, 80–85.

Zhang, F., C. Snyder, and J. Sun, 2004: Impacts of initial estimate and observation availability on convective-scale data assimilation with an ensemble Kalman filter. *Mon. Wea. Rev.*, **132**, 1238–1253.

Zhuang, N., N. Wu, J. Min, and Y. Xu, 2020: Understanding the predictability within convection-allowing ensemble forecasts in east China: Meteorological sensitivity, forecast error growth and associated precipitation uncertainties across spatial scales. *Atmosphere*, **11**, 234, doi:10.3390/atmos11030234.

Zupanski, M., 2005: Maximum likelihood ensemble filter: Theoretical aspects. *Mon. Wea. Rev.*, **133**, 1710–1726.

List of Figures

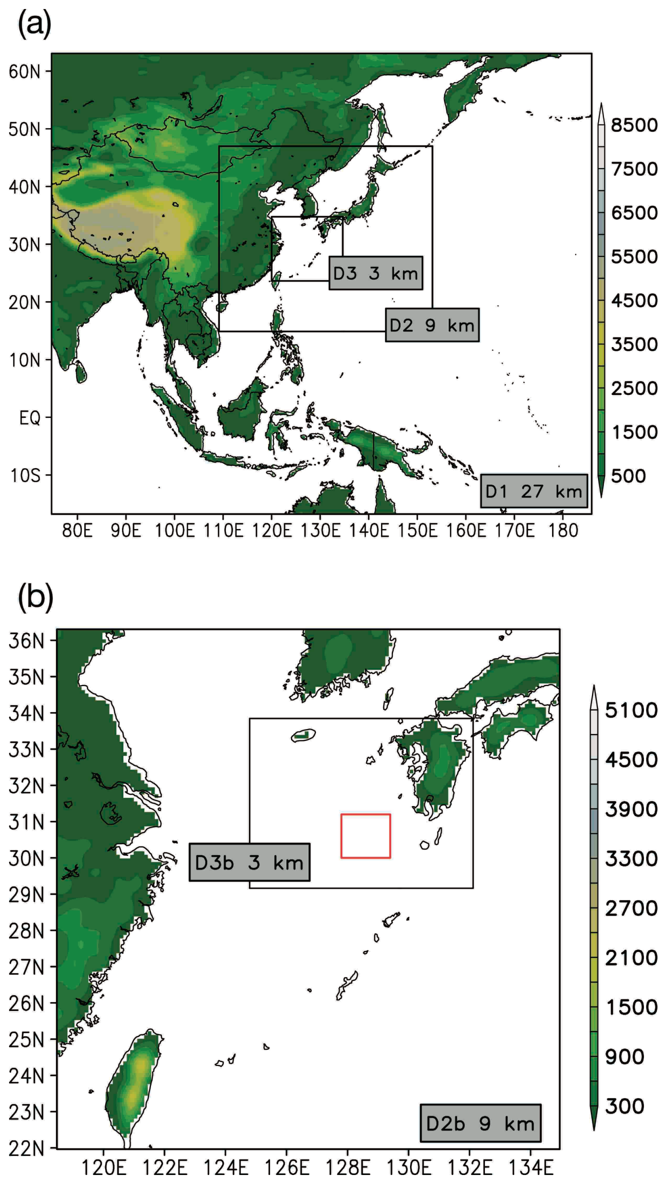

Fig. 1. Computational domains with model terrain heights (m) for (a) ensemble simulations (D1–3) and (b) assimilation experiments (D2b, D3b). Red box in (b) indicates the observation area of the three vessels.

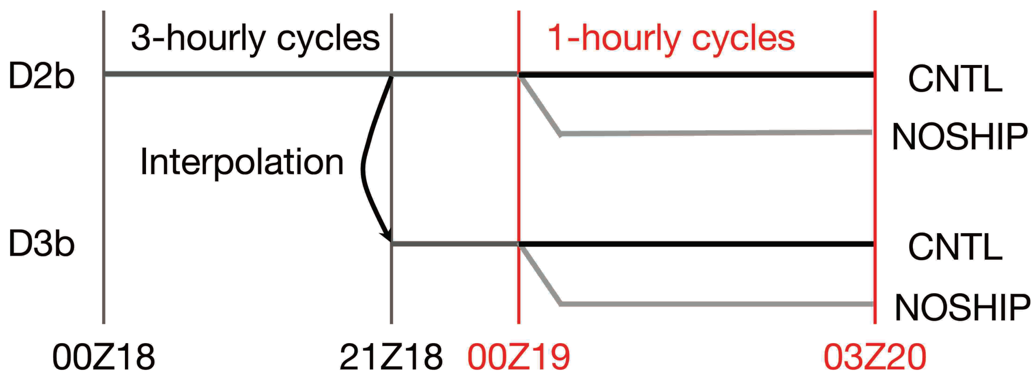

Fig. 2. Schematic diagram for assimilation cycles. The three-hourly cycles in the two domains (D2b, D3b) begin at 0000 UTC on the 18th and 2100 UTC on the 18th, respectively. The hourly CNTL and NOSHIP cycles in D2b and D3b start at 0000 UTC on the 19th and end at 0300 UTC on the 20th.

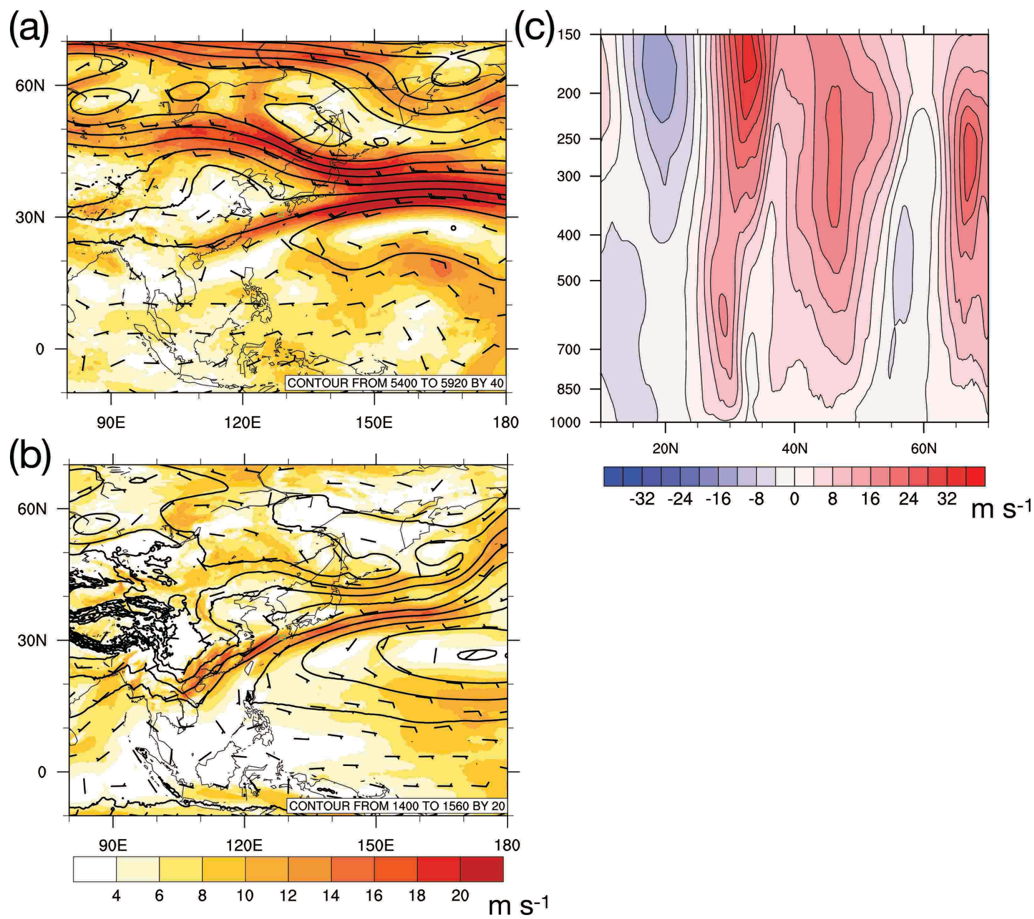

Fig. 3. Large-scale environmental fields of the NCEP GSM initial analysis averaged from 0000 UTC 18 to 1200 UTC 20 June 2022. Horizontal wind speed ($\mathrm{m\,s^{-1}}$, color) and geopotential height (gpm, contour) on the (a) 500 hPa and (b) 850 hPa surfaces; (c) meridional cross section of zonal winds ($\mathrm{m\,s^{-1}}$) averaged from 125°E to 130°E.

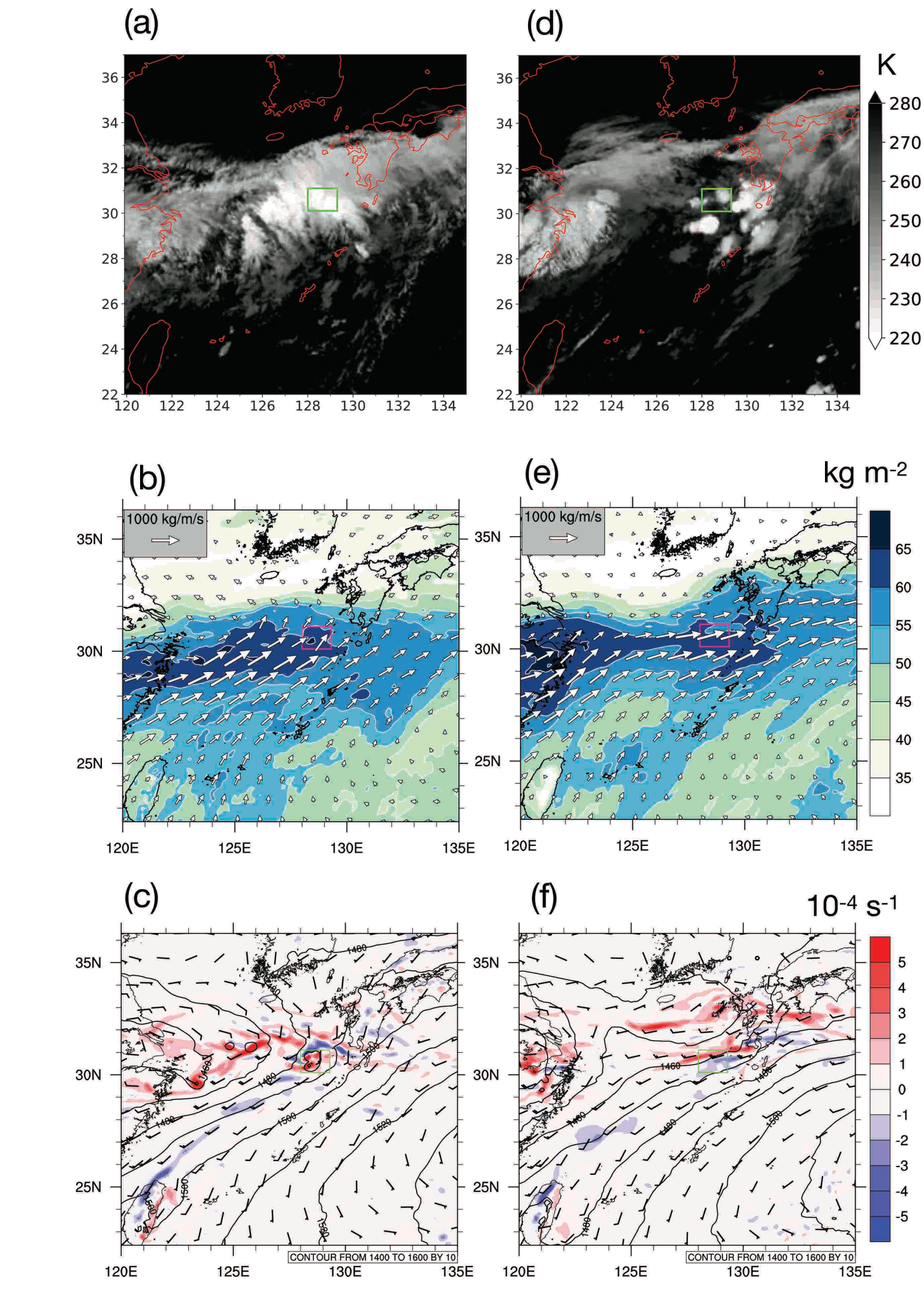

Fig. 4. Environmental features at (a–c) 0300 UTC and (d–f) 2100 UTC 19 June 2022. (a, d) Brightness temperature (K) at the cloud-top (channel 13) of Himawari-8. (b, e) Vertically integrated water vapor flux (scale located upper left, vector) and precipitable water (kg m^{-2}, color), and (c, f) relative vorticity (10^{-4} s^{-1}, color) and geopotential height (gpm, contour) at the 850 hPa surface from the JMA-MA. A Box in each plot indicates the vessel observation area.

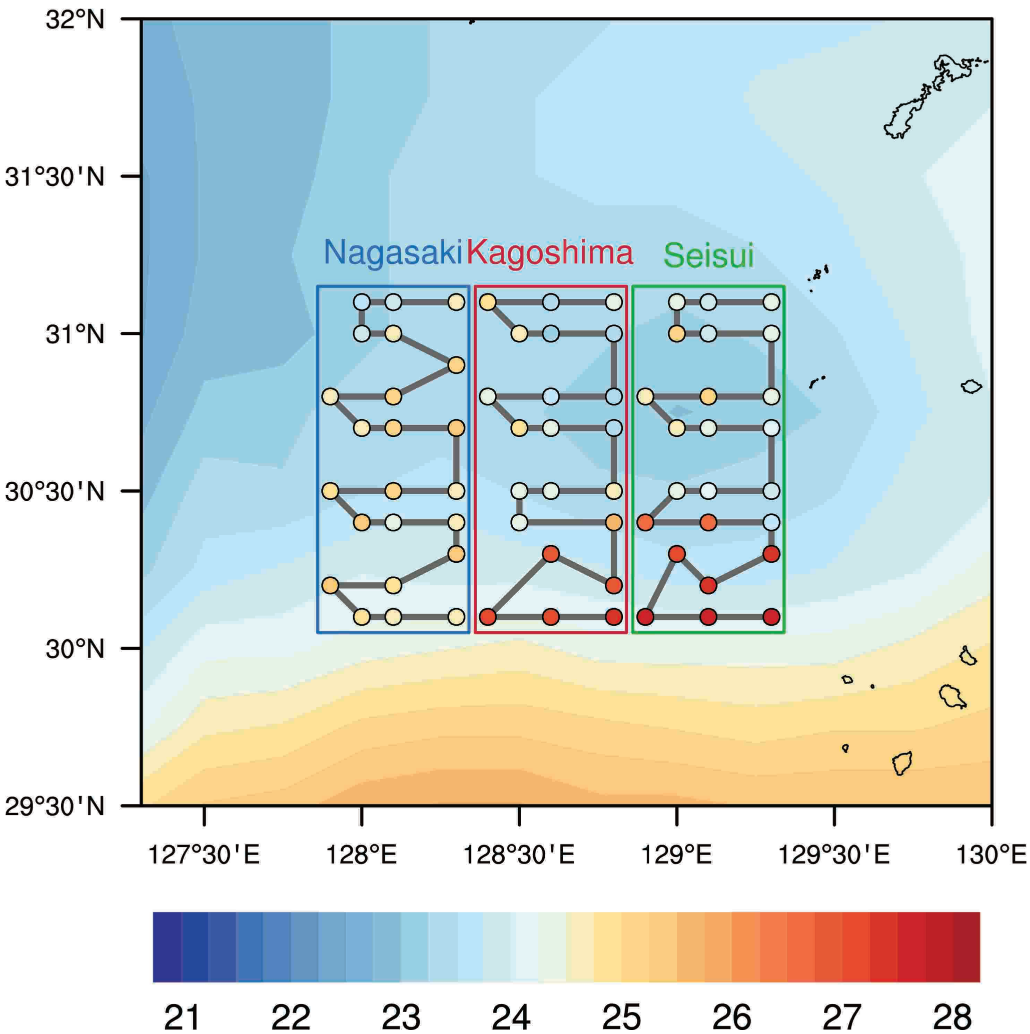

Fig. 5. Sea surface temperature (°C) prescribed in assimilation experiments and observed by the three vessels (circles). Gray lines show the ship tracks.

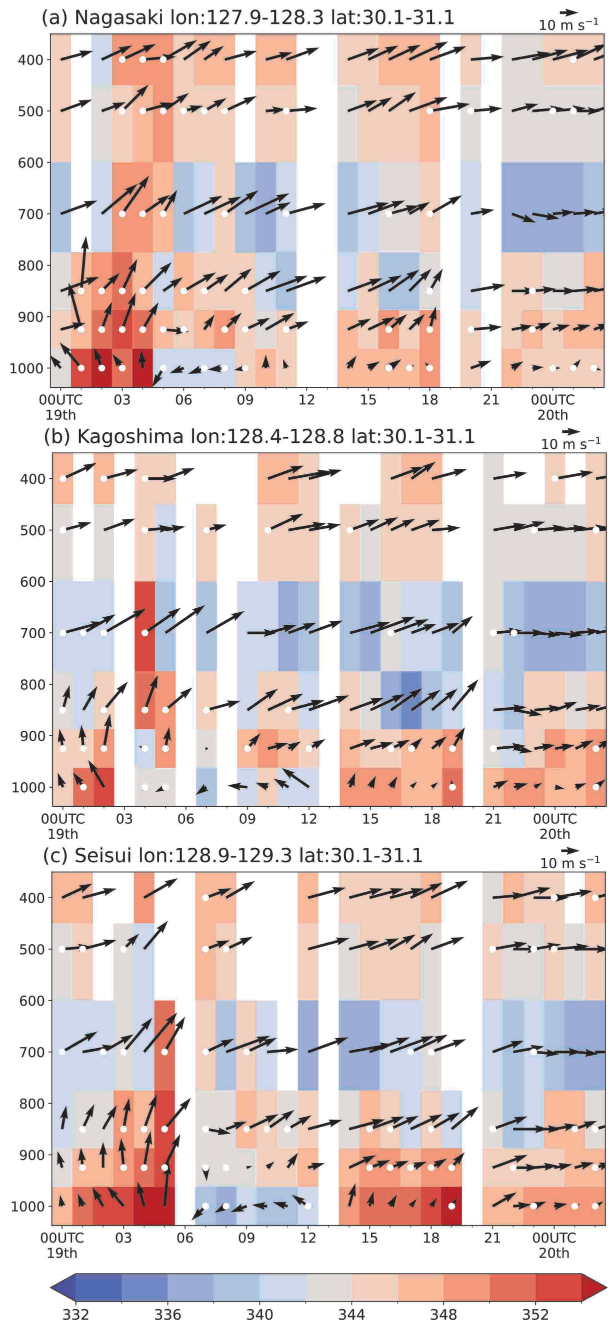

Fig. 6. Time–height cross sections of θ_e (K, color) and horizontal wind ($\mathrm{m\,s^{-1}}$, arrows) at the observation locations of (a) Nagasaki-maru (between 127.9°E and 128.3°E), (b) Kagoshima-maru (between 128.4°E and 128.8°E) and (c) Seisui-maru (between 128.9°E and 129.3°E). The arrow scale is shown in the upper right corner. White dots indicate the layers in which the relative humidity is over 95%.

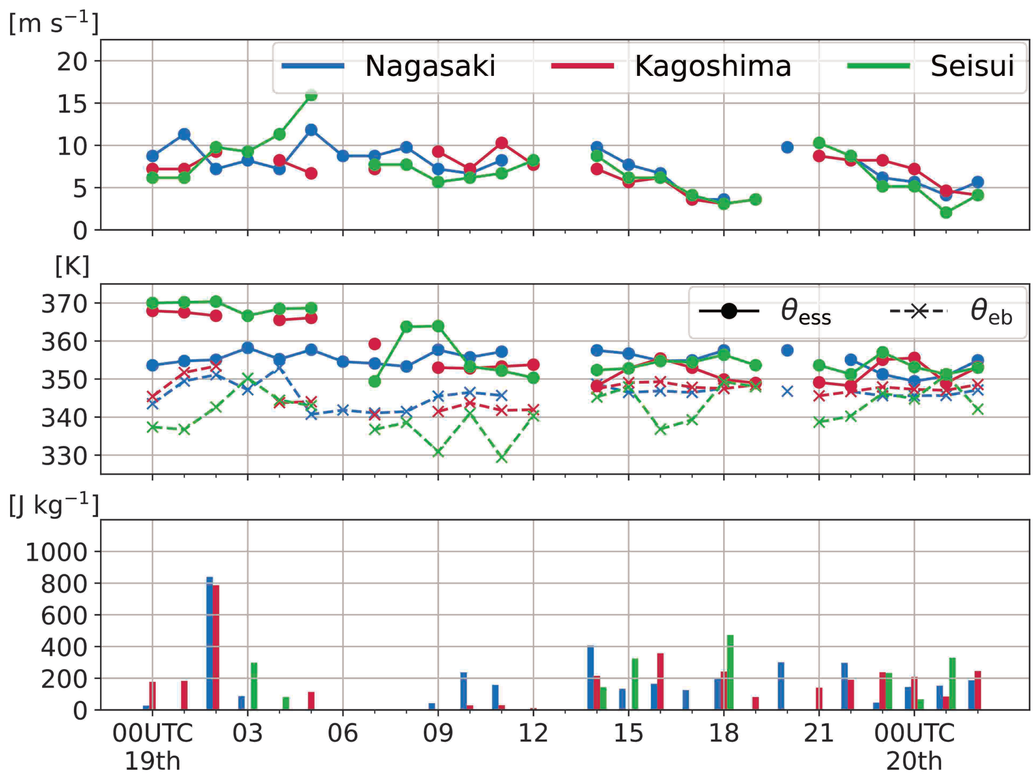

Fig. 7. Surface wind speed (m s^{-1}, top panel), θ_{ess} (solid) and θ_e on the deck (dashed, middle panel), and CAPE (J kg^{-1}, bottom panel) observed by the vessels.

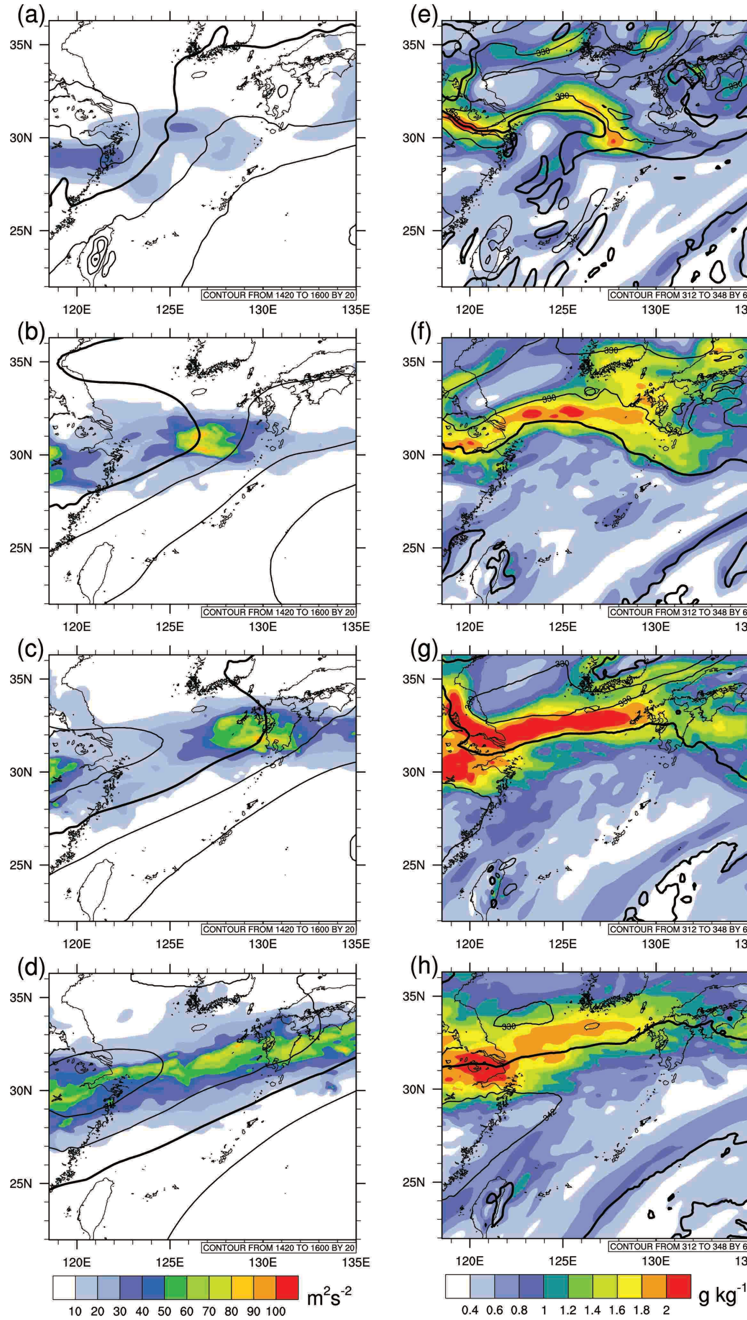

Fig. 8. Ensemble spread in D2 every 12 hours from the initial time to the 36-h forecast. (a) Kinetic energy spread ($\mathrm{m}^2\,\mathrm{s}^{-2}$, color) and the ensemble mean geopotential height (gpm, contour) and (b) specific humidity spread ($\mathrm{g\,kg}^{-1}$, color) and the ensemble mean θ_e (K, contour) at the 850 hPa surface. Thicker contours indicate (a) 1500 gpm and (b) 336 K.

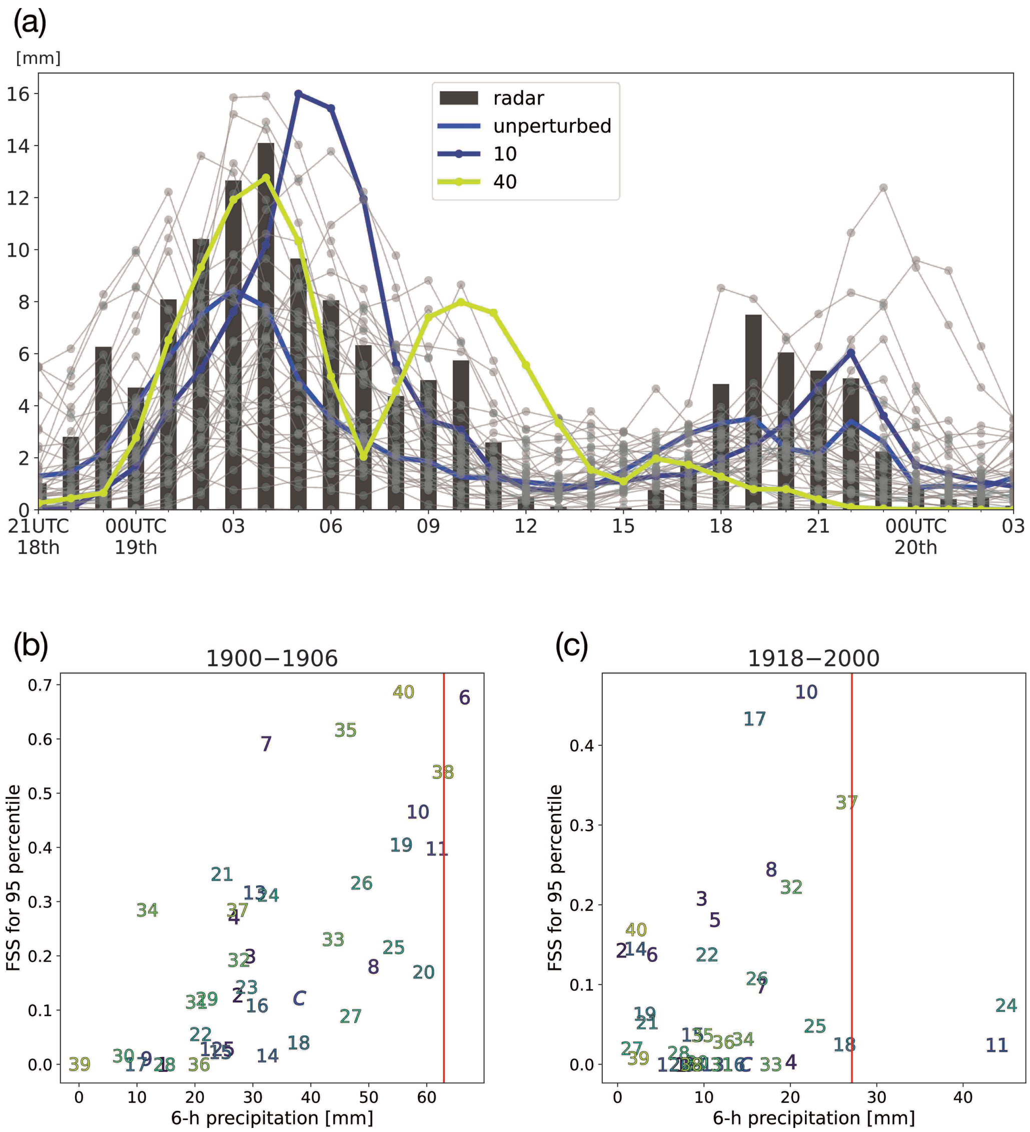

Fig. 9. (a) Precipitation accumulated for the preceding 1-h (mm) averaged in the observation area from 2100 UTC on the 18th to 0300 UTC on the 20th June. The horizontal axis indicates the valid date in UTC. Black bars indicate the precipitation from the JMA radar composite. Blue, dark blue, and yellow-green curves show the unperturbed run, member 10 and 40 in D3, respectively. Gray curves show the other ensemble members. (b, c) Fractions Skill Score (ordinate) and accumulated precipitation in the observation area (mm, abscissa). The mark "c" represents the unperturbed run. Red vertical lines show 6-h precipitation in the observation area obtained from the JMA radar composite. (b) 0000 to 0600 UTC on the 19th and (c) 1800 UTC on the 19th to 0000 UTC on the 20th.

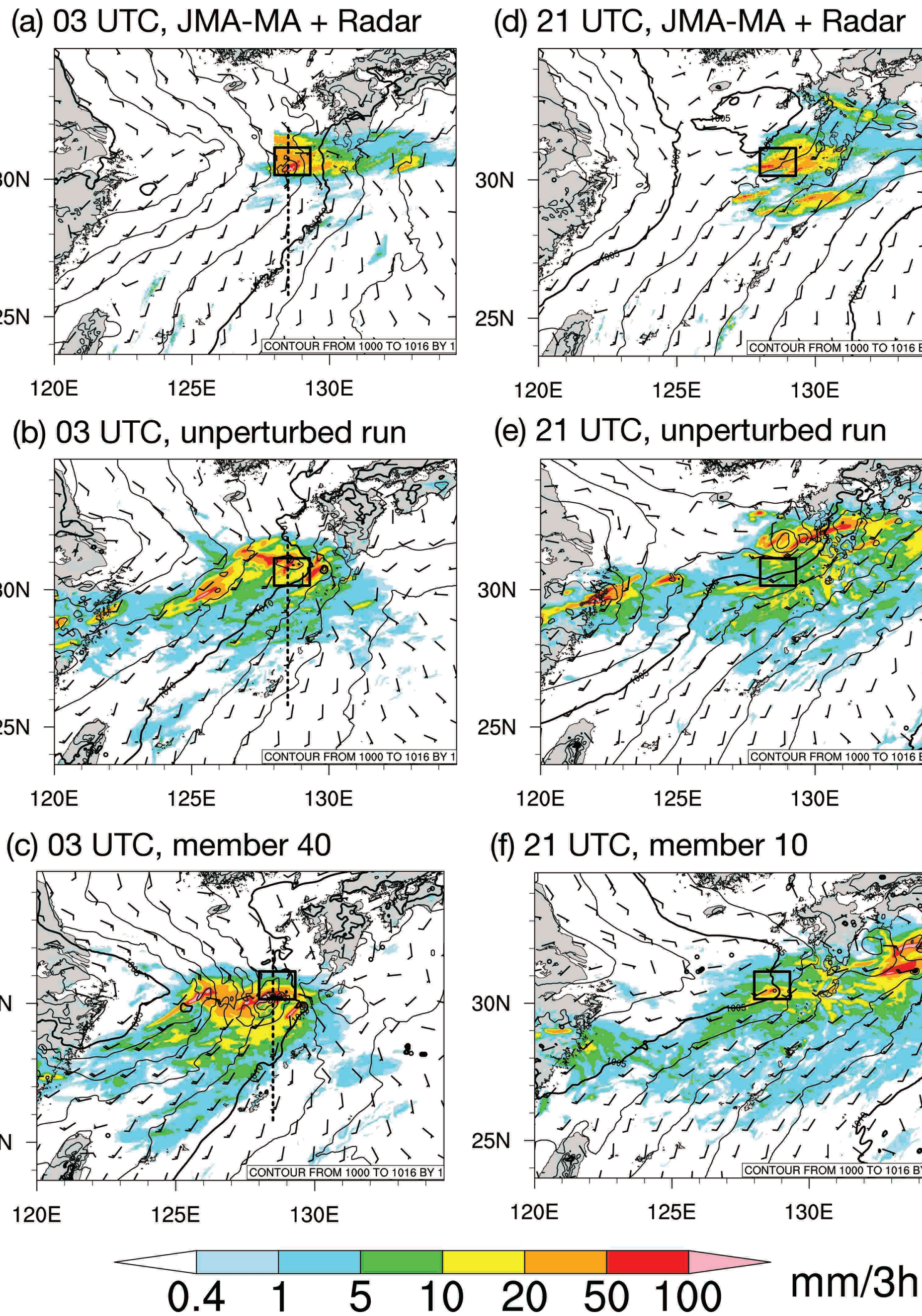

Fig. 10. Mean sea level pressure (contour, per 1 hPa), surface winds (wind barbs) and accumulated precipitation during preceding 3-h (color, mm) at (a–c) 0300 UTC and (d–f) 2100 UTC 19 June. (a, d) The JMA-MA (sea level pressure and winds) and the JMA radar composite, (b, e) the unperturbed run, (c) member 40 and (f) member 10 in D3. Black boxes indicate the observation area.

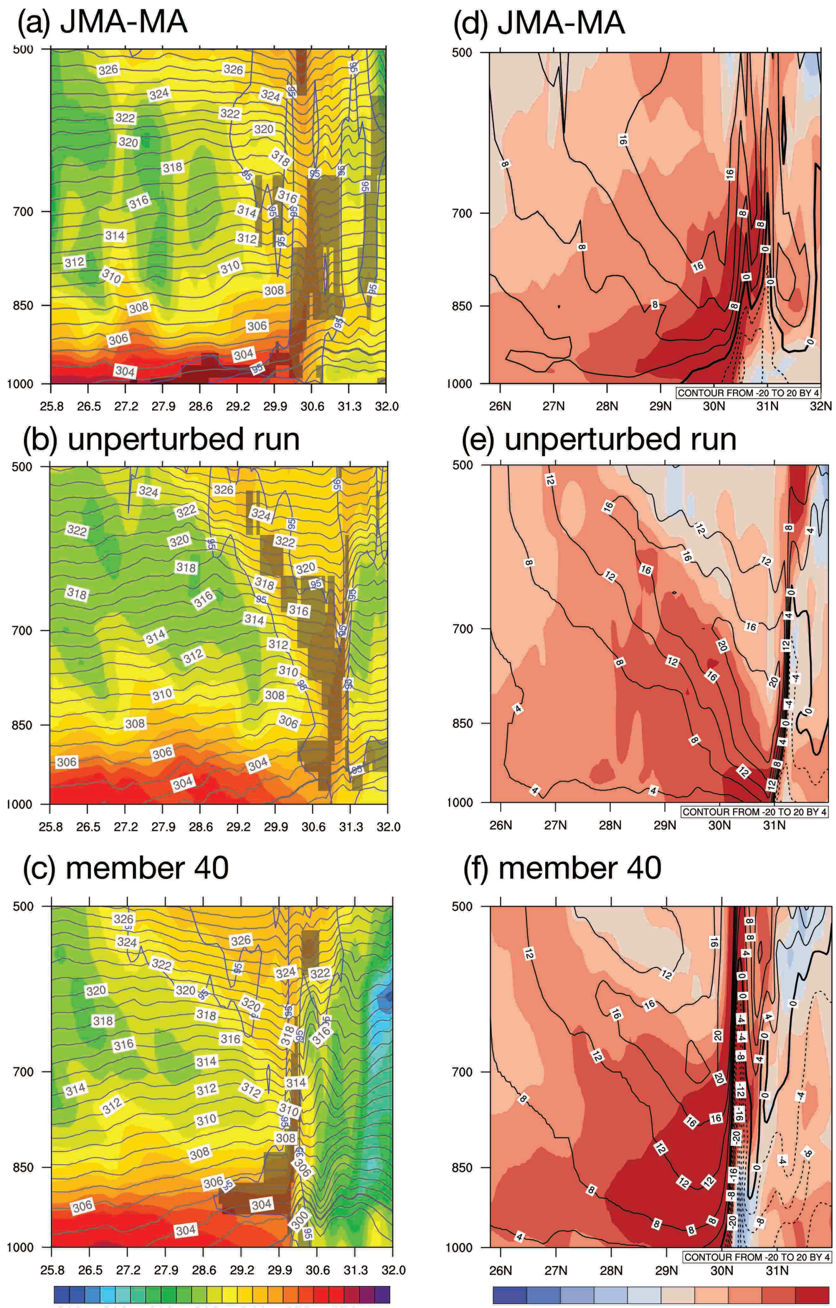

Fig. 11. Meridional cross sections at dashed lines in Fig. 10a–c at 0300 UTC 19 June. (a–c) θ_e (color, K), virtual θ (gray contour, per 1 K), 95% relative humidity (blue contour), MAUL (gray shades), and (d–f) zonal winds (contours in 4 $\mathrm{m\,s^{-1}}$ interval) and meridional winds ($\mathrm{m\,s^{-1}}$, color shades). For zonal winds, negative contours are dashed, and zero contours are thicker than the others. (a, d) The JMA-MA, (b, e) the unperturbed run and (c, f) member 40 in D3.

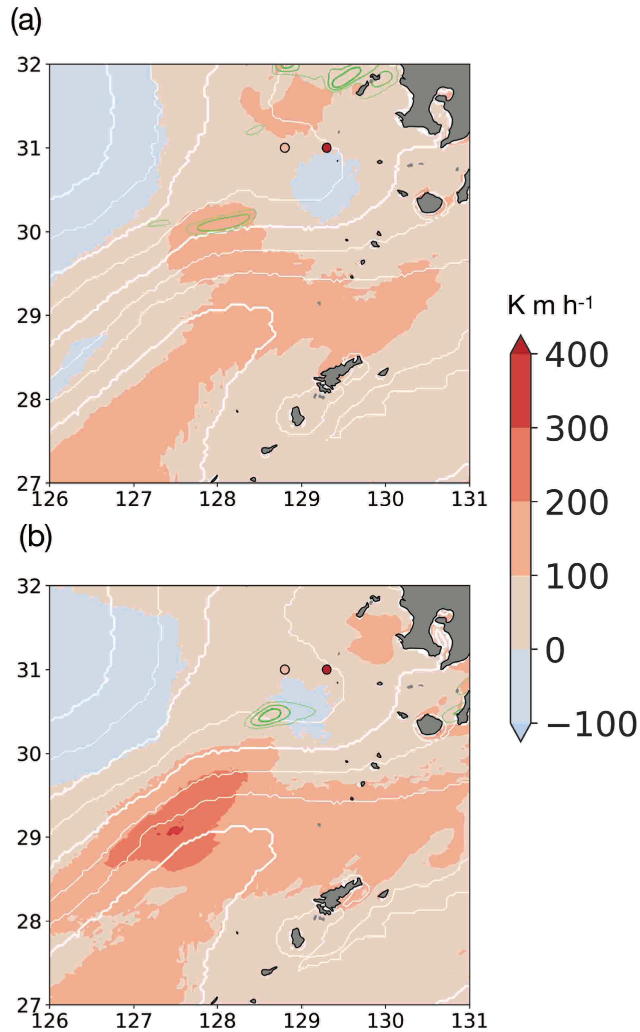

Fig. 12. F_{es} ($\mathrm{K\,m\,h^{-1}}$, color) and θ_{ess} (white contours, interval 3 K) at 2100 UTC 19 June for (a) the unperturbed run and (b) member 10 in D3. The values calculated from the observations by two vessels (Seisui-maru and Kagoshima-maru, Nagasaki-maru is missing) are marked by circles. Green contours indicate the preceding 1-h precipitation amount (8, 16, and 32 mm).

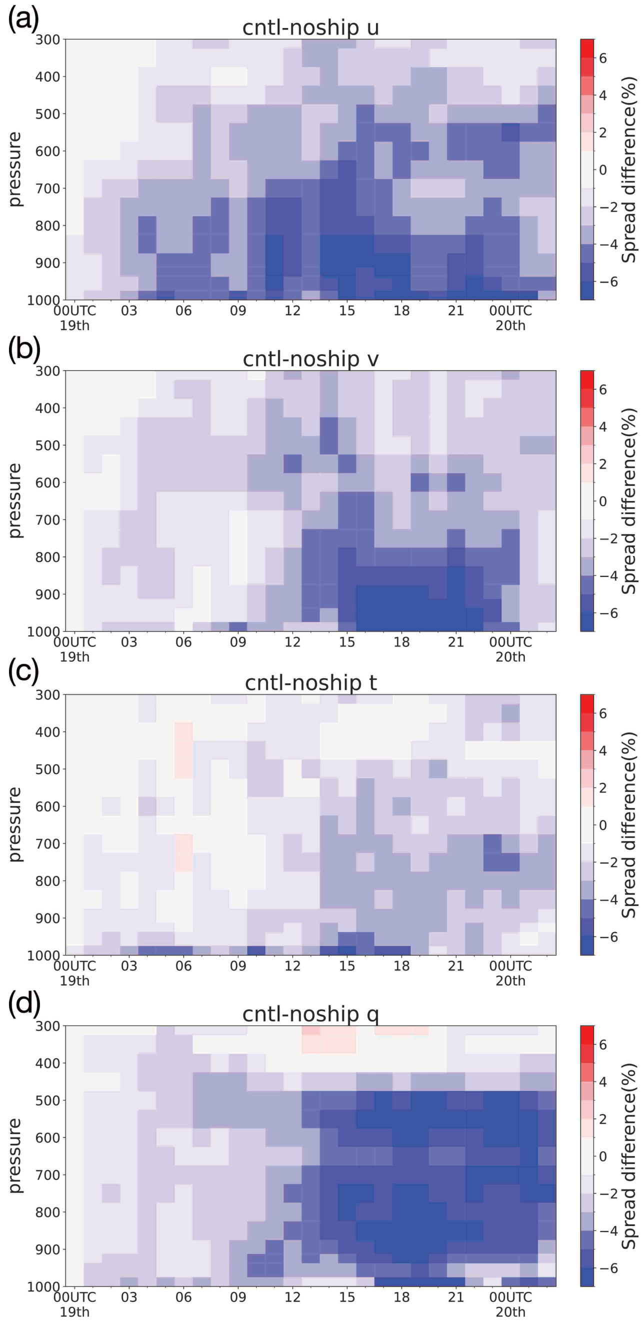

Fig. 13. Time–height cross sections of the difference of analysis ensemble spread (%) of CNTL from NOSHIP averaged in D2b for the (a) zonal winds, (b) meridional winds, (c) temperature, and (d) specific humidity.

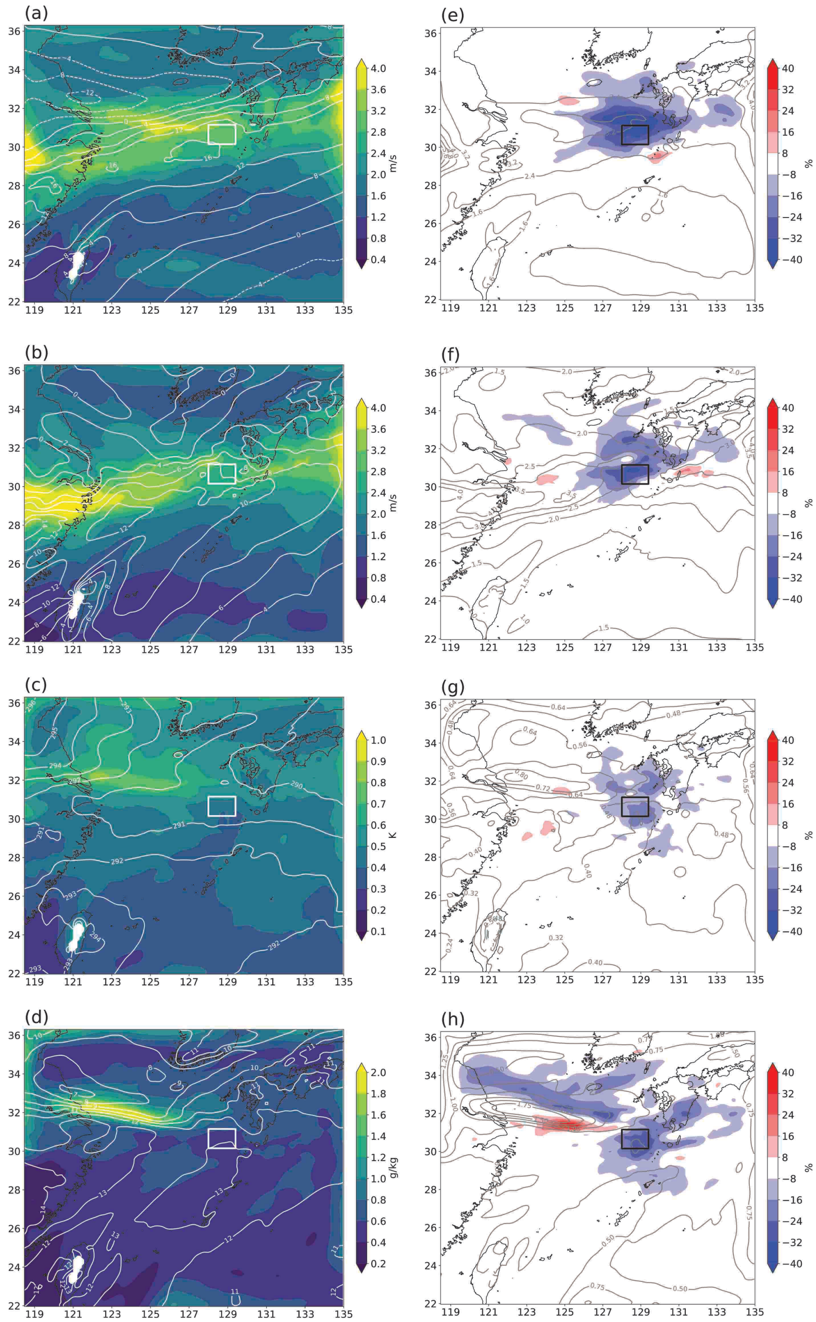

Fig. 14. Time-averaged analysis ensemble spread at the 850 hPa surface of CNTL in D2b for (a) zonal wind, (b) meridional wind, (c) temperature, and (d) specific humidity. White contours show the ensemble mean state of each variable. (e–h) As for (a–d) but showing the difference (%) of CNTL from NOSHIP. Gray contours indicate the ensemble spread of CNTL. Thick white (a–d) or black (e–h) boxes in each panel indicate the observed area.

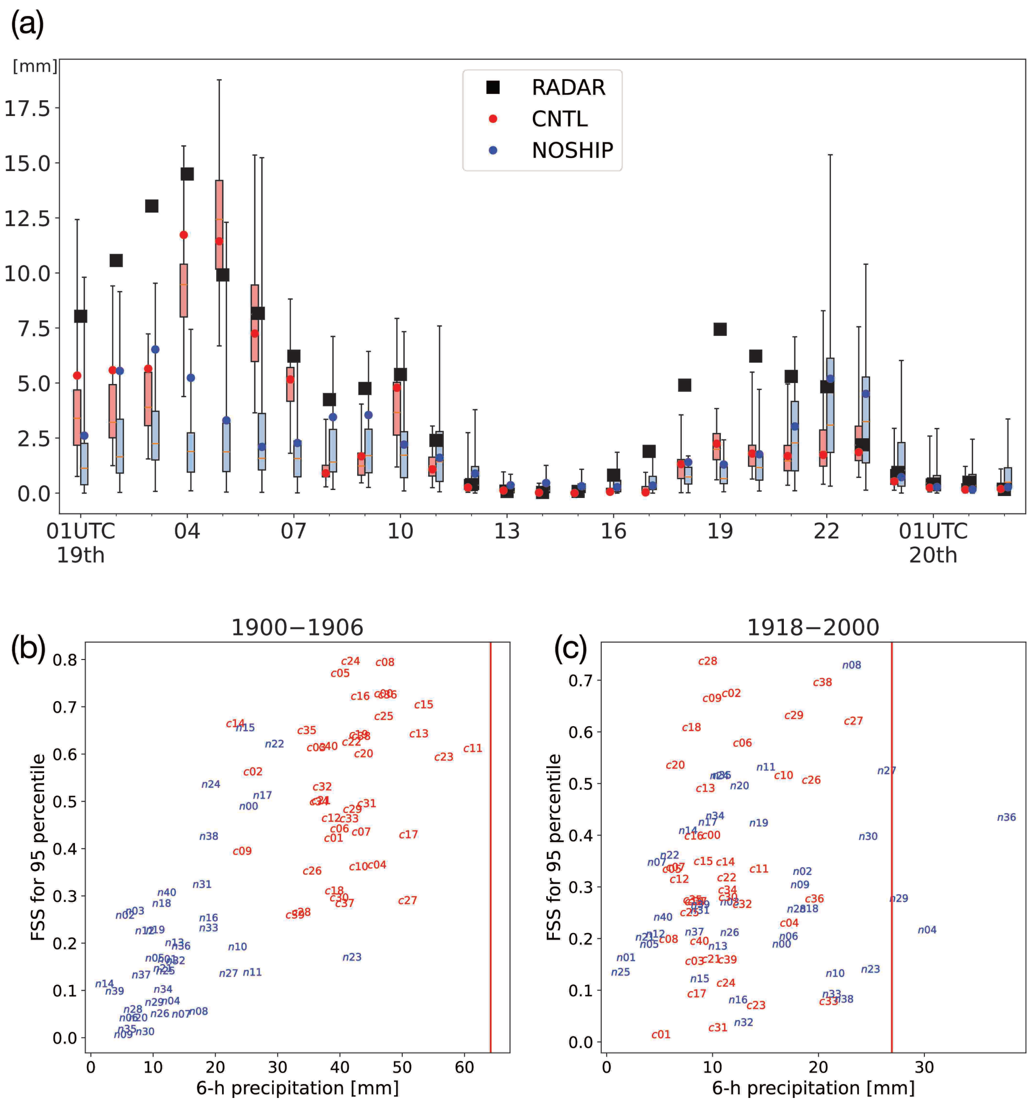

Fig. 15. (a) Boxplots of 1-h accumulated precipitation (mm) averaged in the observation area. The horizontal axis indicates the valid date in UTC. Red (Blue) markers and boxes represent the CNTL (NOSHIP) unperturbed analysis and members in D3b. Black rectangles show the radar composite. (b, c) As in Fig. 9b, c, but for six consecutive cycles of CNTL (red) and NOSHIP (blue).

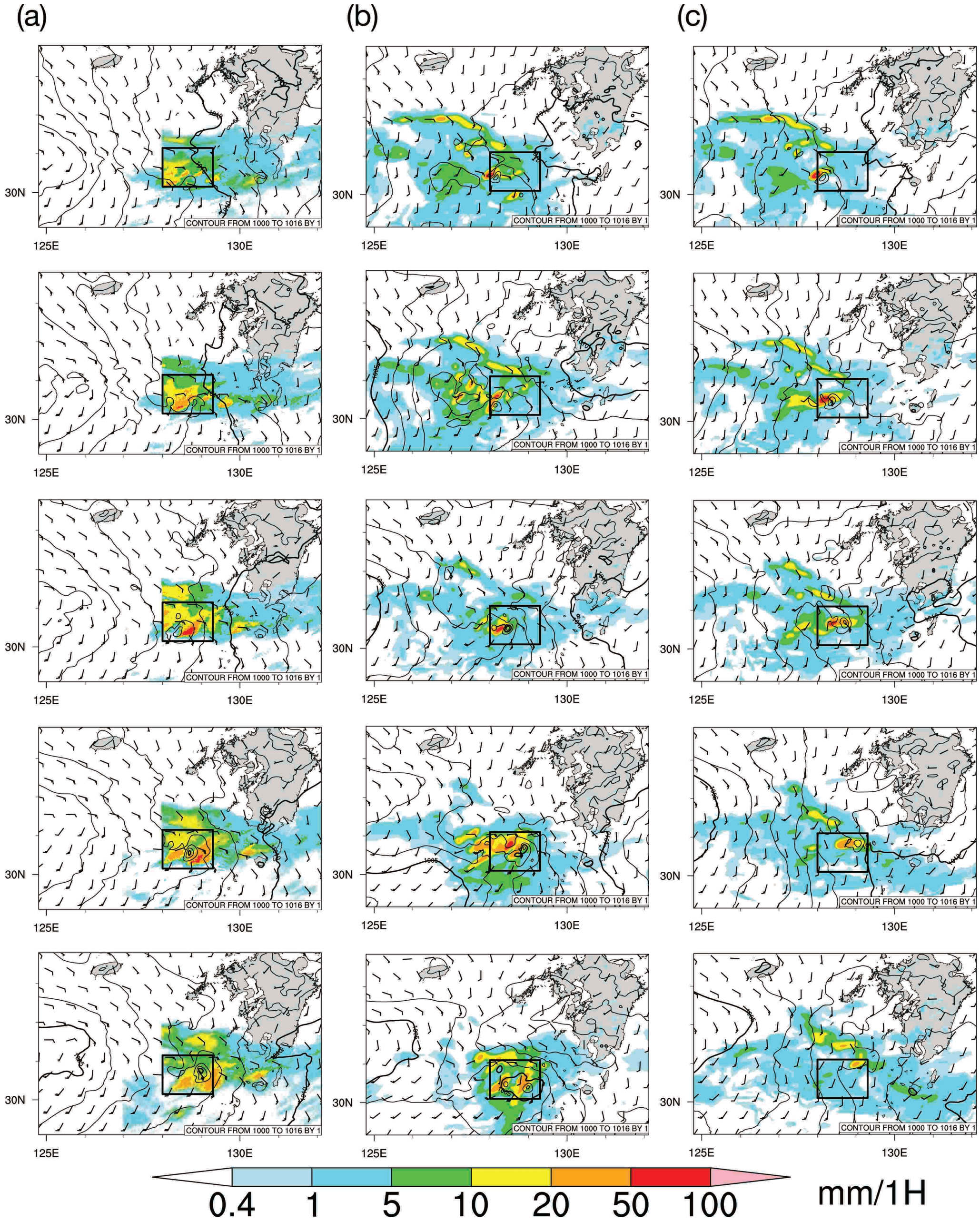

Fig. 16. As in Fig. 10 but for precipitation accumulated for the preceding 1-h from 0100 to 0500 UTC 19 June. (a) The JMA radar composite and the JMA-MA. 1-h forecast from the unperturbed analysis in D3b of (b) CNTL and (c) NOSHIP.

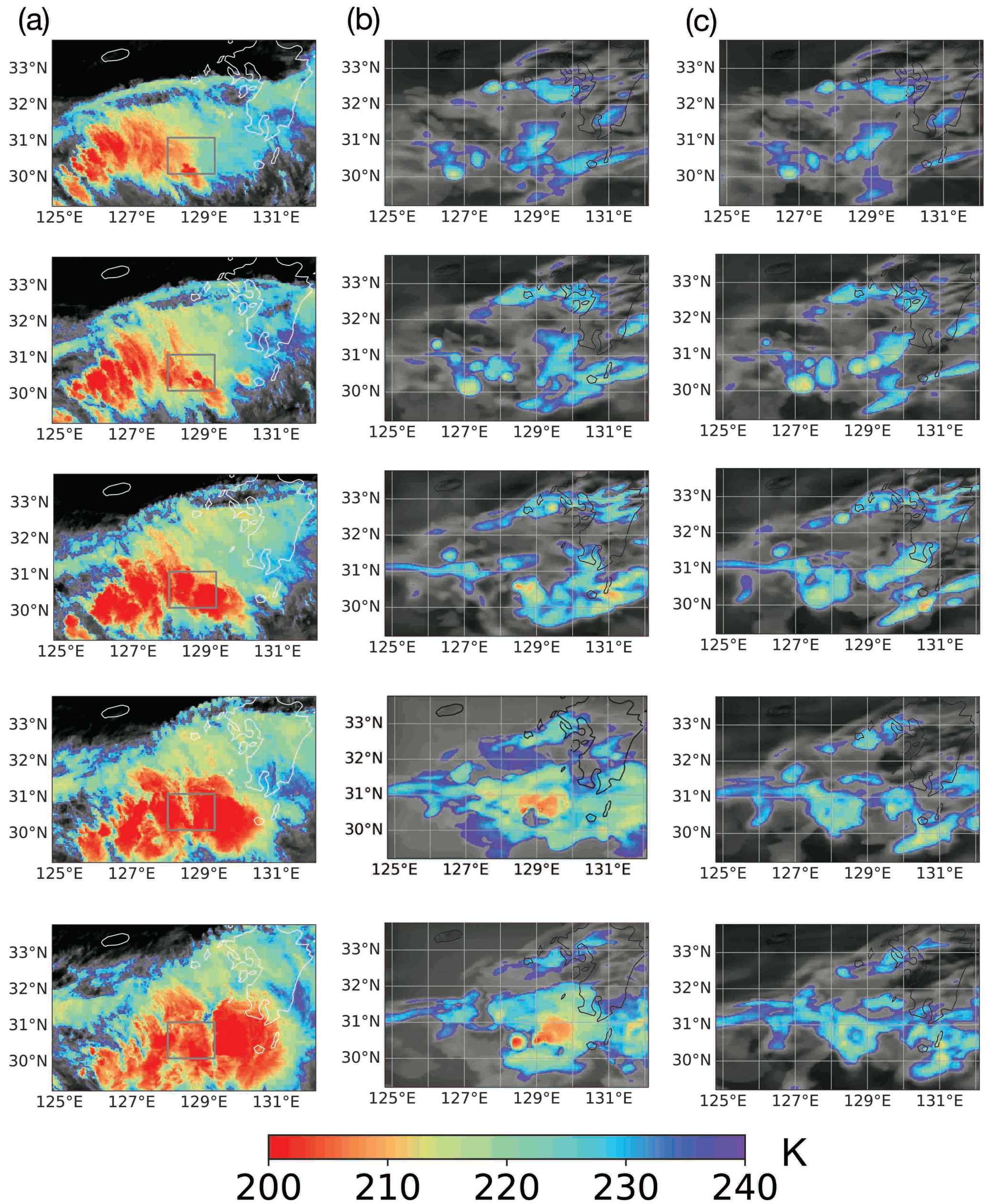

Fig. 17. Comparison of cloud-top brightness temperature (BT, K) from 0100 to 0500 UTC 19 June. (a) Channel 13 of Himawari-8. Simulated BT for 1-h forecast from the unperturbed analysis in D3b of (b) CNTL and (c) NOSHIP.

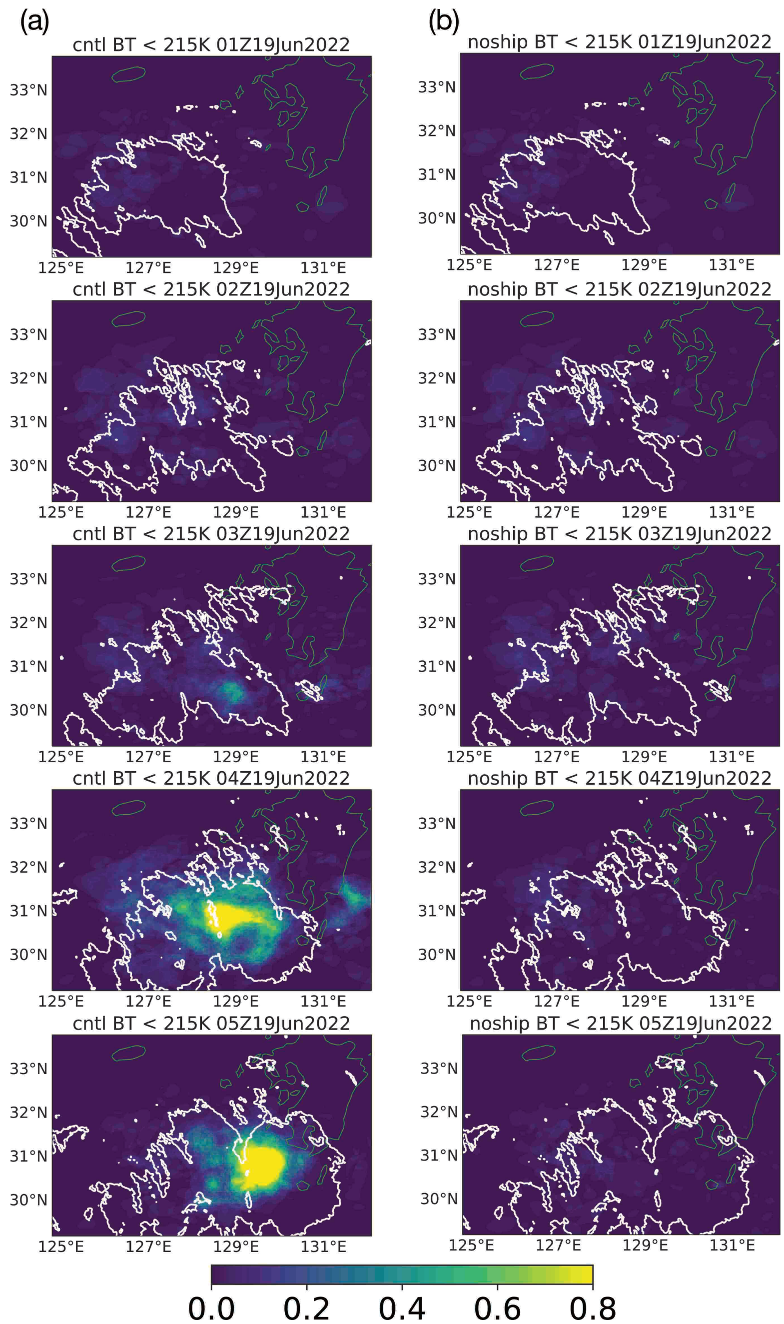

Fig. 18. Ensemble probabilistic forecast of the brightness temperature (BT) from 0100 to 0500 UTC 19 June of (a) CNTL and (b) NOSHIP in D3b. The color of each grid indicates the ratio of the number of members whose BT $<$ 215 K to the ensemble size. White contours show the observed BT of 215 K.

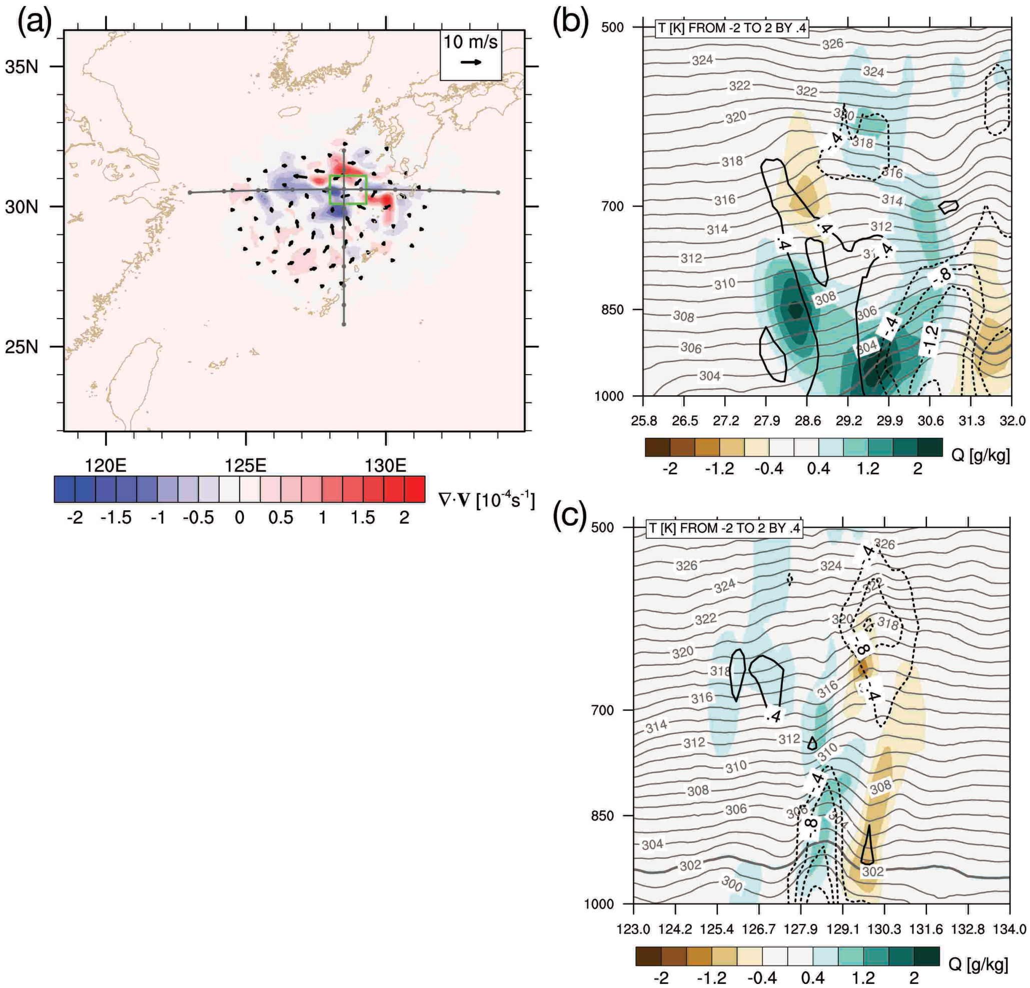

Fig. 19. Incremental difference at 0000 UTC 19 June (the first cycle) between CNTL and NOSHIP in D2b. (a) Horizontal wind (scale located in upper right, vector) and divergence ($10^{-4}\,\mathrm{s}^{-1}$, color) at the 950 hPa surface. (b) Meridional and (c) zonal cross sections shown in (a) for temperature (K, contour, dashed curves are negative) and specific humidity ($\mathrm{g\,kg}^{-1}$, color). Gray contours show the analysis of virtual θ (K).

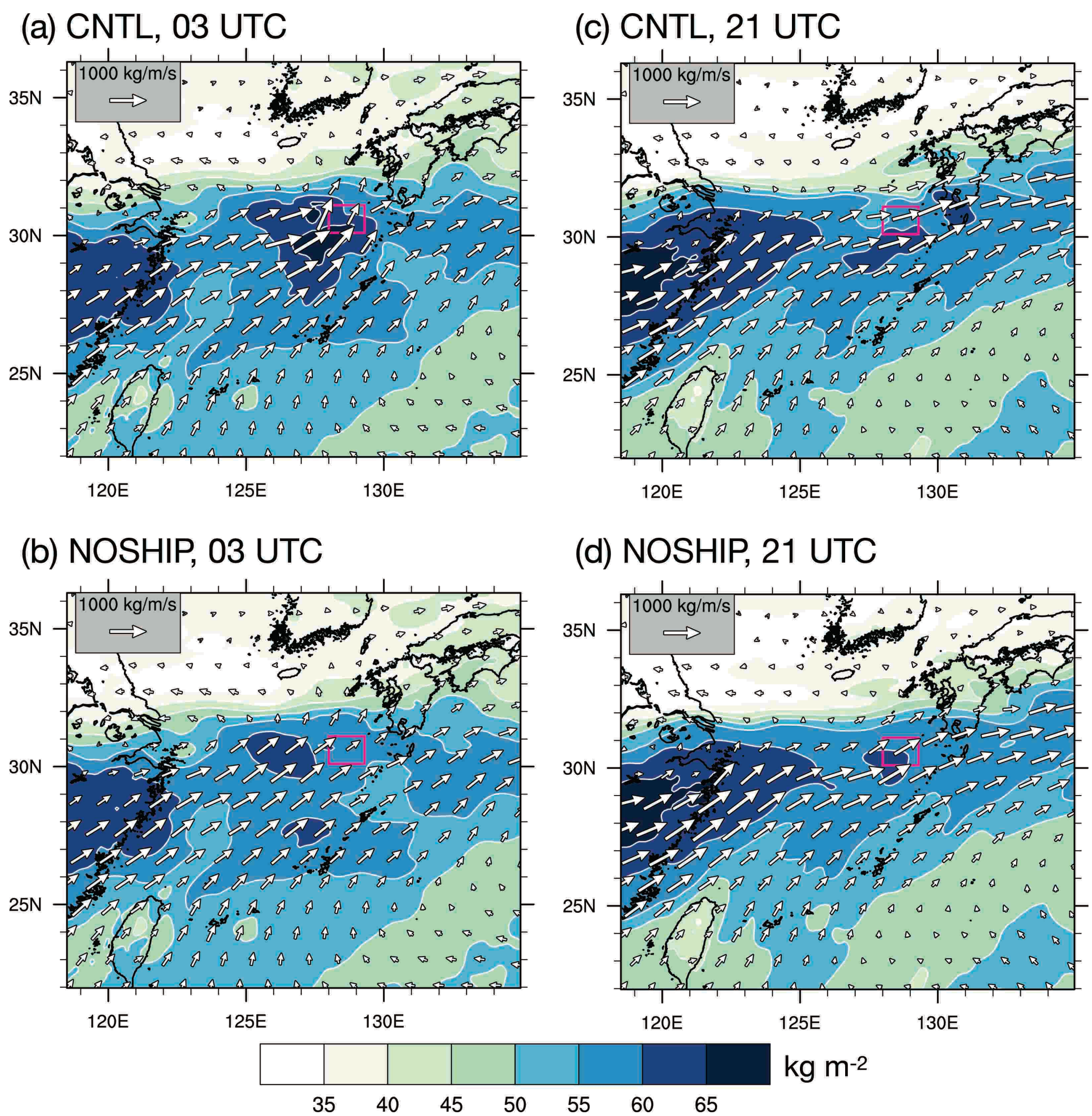

Fig. 20. As in Fig. 4b, e but for the ensemble mean state at (a, b) 0300 UTC (the fourth cycle) and (c, d) 2100 UTC (the 22th cycle) 19 June in D2b of (a, c) CNTL and (b, d) NOSHIP.

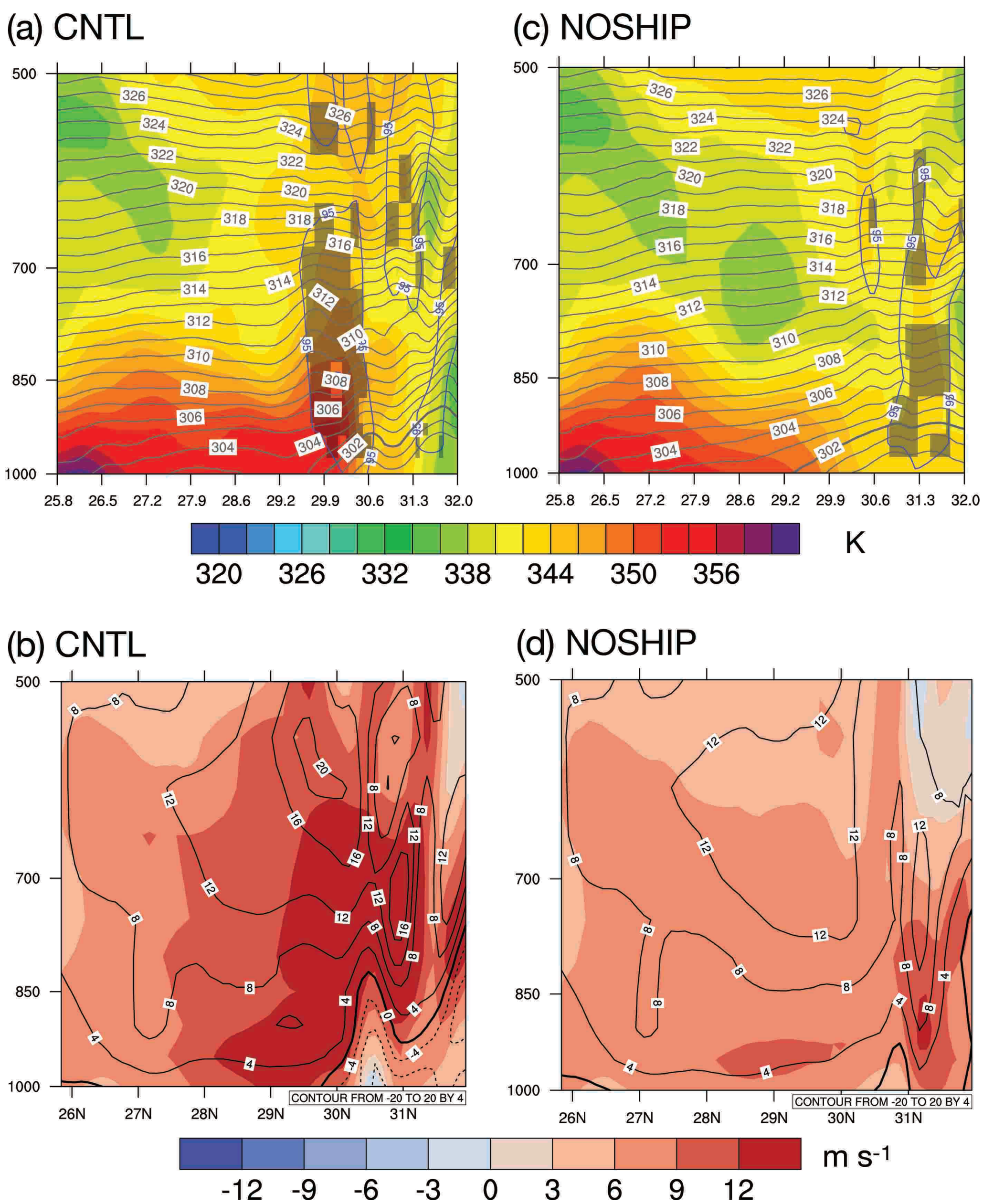

Fig. 21. As in Fig. 11 but for the ensemble mean state at 0300 UTC 19 June (the fourth cycle) in D2b. (a, b) CNTL and (c, d) NOSHIP.

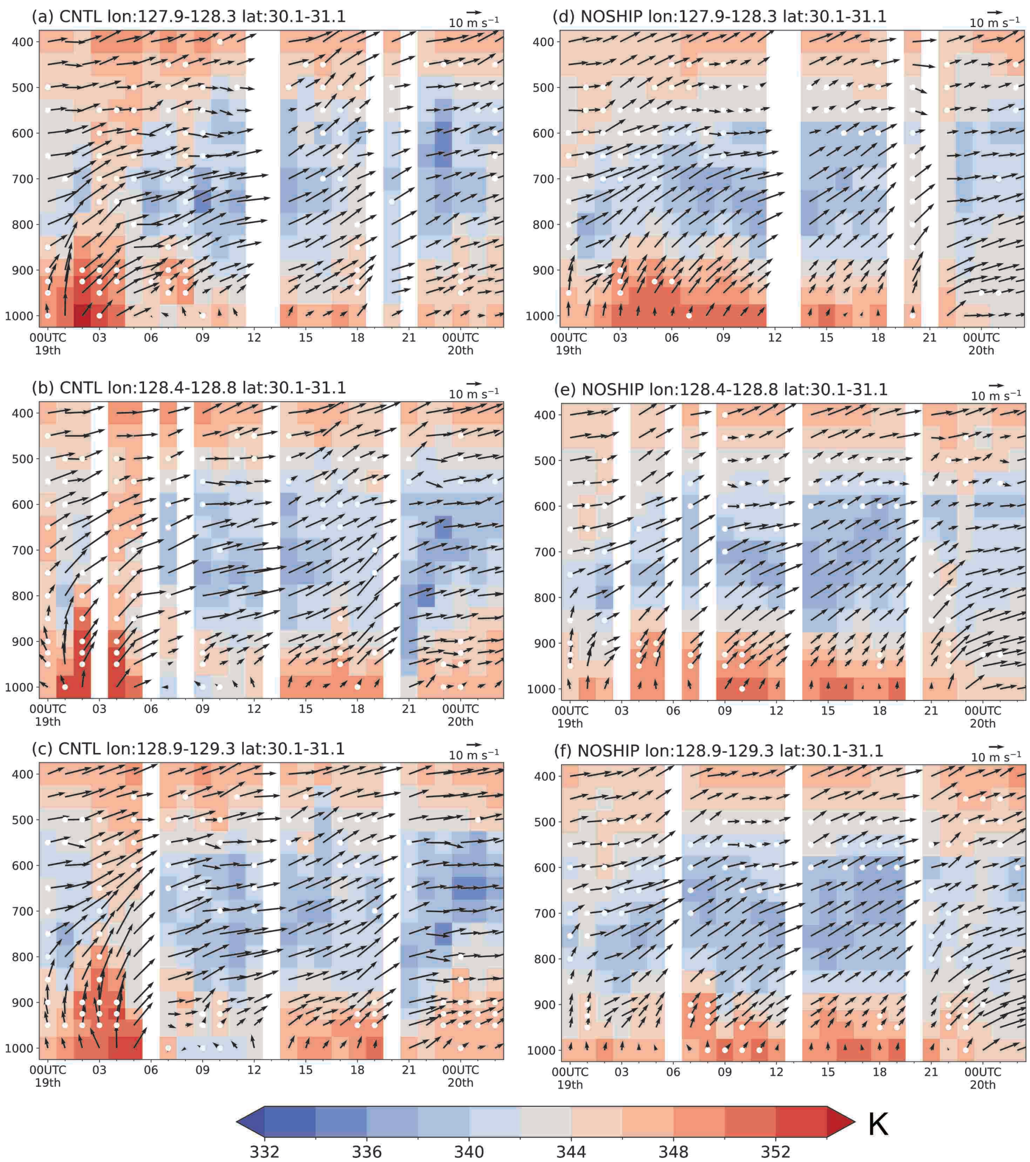

Fig. 22. As in Fig. 6 but for virtual samplings from (a–c) CNTL and (d–f) NOSHIP in D3b.

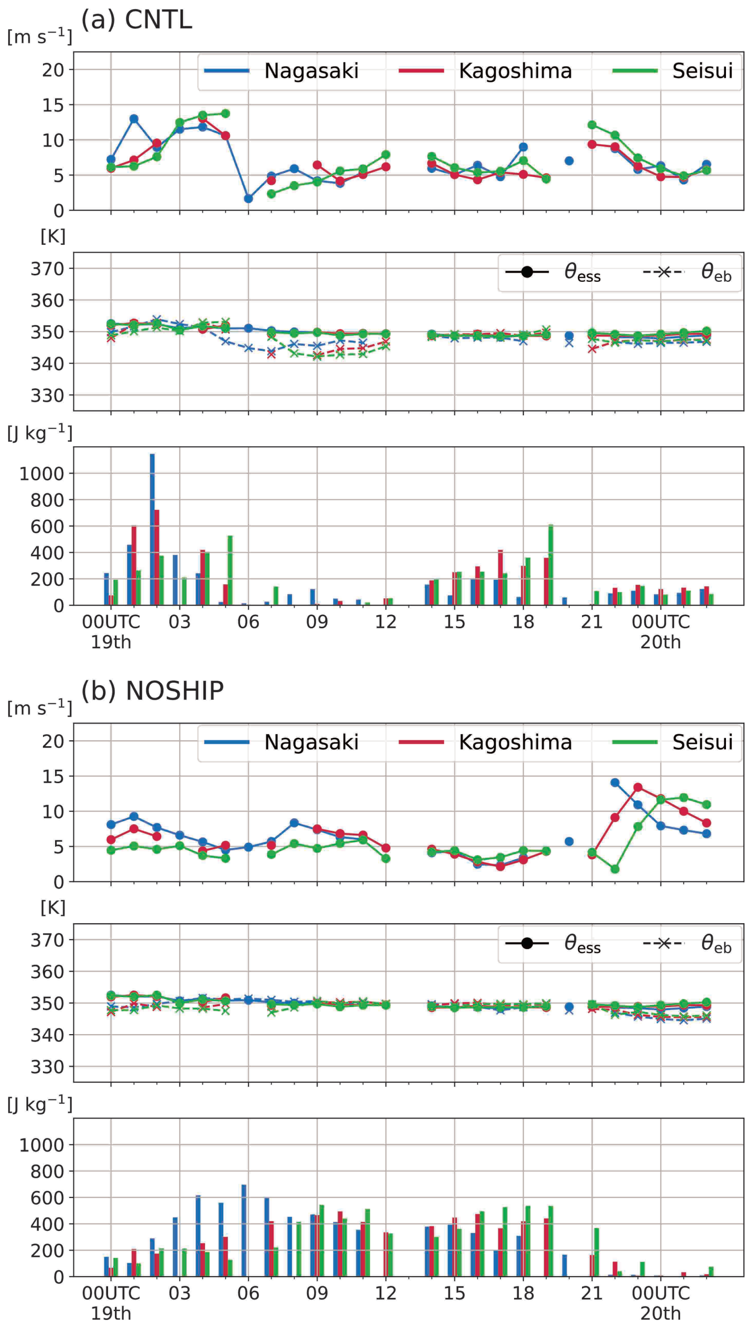

Fig. 23. As in Fig. 7 but for virtual samplings from (a) CNTL and (b) NOSHIP in D3b.

List of Tables

Physics scheme	Specification
Shortwave radiation	Chou and Suarez (1999)
Longwave radiation	Mlawer et al. (1997)
Cumulus convection	Pan and Wu (1995), Hong and Pan (1998)
Shallow convection	Tiedtke (1983)
Microphysics	Ferrier et al. (2002)
Planetary boundary layer	Hong and Pan (1996)
Orographic gravity wave drags	Kim and Arakawa (1995)
Land surface model	Ek et al. (2003)
Numerical method	
Time filter	Asselin (1972)
Semi-implicit adjustment	Robert et al. (1972), Ikawa (1988)
Implicit lateral boundary relaxation	Tatsumi (1986), Juang and Kanamitsu (1994)

Table 1. Model physics schemes and numerical methods used in NCEP RSM and MSM.